Geochemistry Geophysics Geosystems G3
AN ELECTRONIC JOURNAL OF THE EARTH SCIENCES
Published by AGU and the Geochemical Society

Article
Volume 5, Number 11
13 November 2004
Q11009, doi:10.1029/2004GC000701
ISSN: 1525-2027

Physical response of mid-ocean ridge hydrothermal systems to local earthquakes

William S. D. Wilcock
School of Oceanography, University of Washington, Box 357940, Seattle, Washington 98115, USA (wilcock@u.washington.edu)

[1] Observations from the East Pacific Rise (EPR) and the Endeavour segment of the Juan de Fuca Ridge show that local earthquake swarms can lead to increased hydrothermal venting temperatures after a delay of several days. I develop two models for this process. In the temperature perturbation model, a new pathway opens to a heat source, and the temperatures of fluids leaving the reaction zone increase. By considering the exchange of heat between the fluid flowing up a conduit and the wall rock, I solve for the resulting perturbation to venting temperatures. For flow in a crack the response is delayed, and the delay increases as the crack narrows or the reaction zone deepens, but for a pipe the venting temperature increases either quickly or barely at all. In the pressure perturbation model, there is a transient increase in pressures at depth due to a decrease in porosity, the release of overpressured fluids, or a readjustment of pressures in response to a change in the relative permeabilities of the upflow and downflow zones. One-dimensional solutions for pressure diffusion show that this model can lead to a delayed increase in outflow fluxes which may be accompanied by increased venting temperatures. The temperature perturbation model fits the data from the EPR event well. The Endeavour event is less well constrained, and both models can fit the observations adequately. Local seismic networks and time series of fluid flux, chemistry, and temperature will be required to fully exploit hydrothermal perturbation events to infer subseafloor hydrology.

Components: 14,838 words, 17 figures, 2 tables.

Keywords: earthquake swarm; hydrothermal system; mid-ocean ridge; venting temperature.

Index Terms: 3015 Marine Geology and Geophysics: Heat flow (benthic) and hydrothermal processes; 3035 Marine Geology and Geophysics: Midocean ridge processes; 8135 Tectonophysics: Hydrothermal systems (8424).

Received 23 January 2004; **Revised** 9 July 2004; **Accepted** 27 July 2004; **Published** 13 November 2004.

Wilcock, W. S. D. (2004), Physical response of mid-ocean ridge hydrothermal systems to local earthquakes, *Geochem. Geophys. Geosyst.*, *5*, Q11009, doi:10.1029/2004GC000701.

1. Introduction

[2] Within the mid-ocean ridge research community there is considerable interest in establishing multidisciplinary observatories on the seafloor. Observatories are necessary to obtain improved observations of the episodic diking-eruptive events and earthquakes responsible for the formation of oceanic crust and the effects of such episodic events on hydrothermal systems and the chemosynthetic biological communities they support. One potential application of observatory data is to treat well-characterized volcanic or tectonic events as natural perturbation experiments and develop models to interpret the hydrothermal response at the seafloor in terms of subsurface hydrological properties and the geometry of hydrothermal flow.

[3] To date, only one seafloor observatory has been established on a mid-ocean ridge [*Embley and Baker*, 1999] and only a handful of shorter-term

experiments have focused on multidisciplinary time series observations. As a result there are still relatively few observations that document the immediate effect of volcanic and tectonic events on hydrothermal venting. Over the past 15 years, a number of seafloor eruptions have been detected either fortuitously or through remote seismic monitoring [*Cowen et al.*, 2004]. One important result of follow up cruises has been the discovery of event plumes (or megaplumes) at many sites. These are large hydrothermal plumes that rise ~1 km above the seafloor [*Baker et al.*, 1987]. Their formation mechanism is controversial and they are alternatively attributed to the release of a subsurface reservoir of chemically mature hydrothermal fluids or the flash heating of seawater by shallow intrusions and/or lava flows [e.g., *Palmer and Ernst*, 1998; *Lupton et al.*, 1999b; *Palmer et al.*, 2000, and references therein]. However, the rise heights and chemistry suggest that they form in a matter of hours to days [*Baker et al.*, 1989; *Lavelle*, 1995] and very soon after the causative volcanic event [e.g., *Baker et al.*, 1995; *Massoth et al.*, 1995].

[4] These inferences are supported by data from the 1998 eruption at Axial Seamount on the Juan de Fuca Ridge, the only mid-ocean ridge eruption to be recorded by in situ instruments [*Embley and Baker*, 1999]. Temperatures measured on the seafloor and in the water column increased ~4 hours after onset of seismic activity [*Baker et al.*, 1999] and simultaneously with the onset of caldera deflation [*Fox*, 1999] before declining over about two weeks. No event plume was found at this site by a follow-up cruise that arrived on site 18 days later [*Baker et al.*, 1999] but the ^{3}He/heat ratios of the first fluids sampled were similar to other event plumes [*Lupton et al.*, 1999a]. It seems likely that the event plume had either migrated off-axis or did not form because of strong ocean currents [*Lupton et al.*, 1999a].

[5] In addition to the observations following eruptions, there are two well-documented examples of the hydrothermal response to noneruptive earthquake swarms. The two swarms had very different characteristics but each was characterized by a hydrothermal response that was delayed by several days. In 1995 on the East Pacific Rise (EPR) near 9°50′N, a swarm of >100 small microearthquakes was followed four days later by the onset of a 7°C increase in vent temperatures at the Bio9 black smoker vent located only a few hundred meters from the earthquake epicenters [*Fornari et al.*, 1998; *Sohn et al.*, 1998]. This was interpreted as a cracking event in which the earthquake swarm opened a pathway to a new heat source and the time delay was equated to the residence time of hydrothermal fluids in the upflow zone [*Fornari et al.*, 1998; *Sohn et al.*, 1998]. In 1999 on the Endeavour segment of the Juan de Fuca Ridge, a much larger swarm comprising over 2500 earthquakes was detected by the SOSUS hydrophone network [*Johnson et al.*, 2000] and included several earthquakes detected by land networks [*Bohnenstiehl et al.*, 2002, 2004]. The onset of seismicity was followed 4–11 days later by temperature increases at several sites of diffuse venting [*Johnson et al.*, 2000] located within the region defined by the scatter of the SOSUS epicenters. The earthquake swarm was initially interpreted as tectonic but subsequent analysis of the swarm characteristics [*Bohnenstiehl et al.*, 2002, 2004] and the chemistry of discrete samples of hydrothermal fluid [*Lilley et al.*, 2003; *Seyfried et al.*, 2003] suggest that it was associated with a volcanic intrusion.

[6] Without discussing the mechanism, *Johnson et al.* [2000] hypothesize that a delay of several days may be a characteristic time constant associated with the reaction of hydrothermal flow to a seismic disturbance. Since continental hydrothermal systems often respond nearly instantaneously to earthquakes, *Dziak and Johnson* [2002] infer that mid-ocean ridge systems behave differently from their land-based counterparts and they hypothesize that this may be due to crustal architecture.

[7] In this paper, I develop two types of quantitative model that can account for a delayed hydrothermal response at the seafloor and which can be used to interpret time series observations in terms of hydrological properties. In the first, a cracking event causes a temperature perturbation at the base of the upflow zone which is then advected to the seafloor. In the second, a variety of mechanisms lead to transient excess pressures at depth in the upflow zone that diffuse to the seafloor while driving increased upflow. I show that the temperature perturbation model can fit the temperature data for the 1995 EPR event remarkably well although it is not possible to entirely discount the pressure perturbation model. The 1999 Endeavour event is less well constrained and both types of model can fit the temperature data well and both may have contributed to the observed response. I conclude that a delayed response is a natural consequence of perturbing a hydrothermal system at depth rather than near the seafloor and I empha-

Table 1. Fluid and Rock Properties

Property	Symbol	Value	Source
		Hot Hydrothermal Fluid	
Bulk modulus[a]	K_f	0.14 Gpa	*Anderko and Pitzer* [1993]
Density[a]	ρ_f	636 kg m^{-3}	*Anderko and Pitzer* [1993]
Heat capacity[a]	c_f	6.4×10^3 J kg^{-1} K^{-1}	*Anderko and Pitzer* [1993]
Temperature[b]	T	365°C	*Fornari et al.* [1998]
Viscosity[a]	μ	7.5×10^{-5} Pa s	*Meyer et al.* [1993]
		Cold Hydrothermal Fluid	
Bulk modulus[a]	K_f	2.3 Gpa	*Anderko and Pitzer* [1993]
Density[a]	ρ_f	1038 kg m^{-3}	*Anderko and Pitzer* [1993]
Temperature[b]	T	2°C	
		Fluid Saturated Rock	
Density	ρ_r	2800 kg m^{-3}	*Carlson and Herrick* [1990]
Porosity[c]	ϕ	0.03	*Becker* [1985]
Drained bulk modulus	K	50 Gpa	*Crone and Wilcock* [2002]
Heat capacity	c_r	1.2×10^3 J kg^{-1} K^{-1}	*Petrunin et al.* [2001]
Thermal conductivity[d]	λ	1.84 J m^{-1} K^{-1}	*Clauser and Huenges* [1995]
Thermal diffusivity	κ	5.5×10^{-7} m^2 s^{-1}	$\lambda/\rho_r c_r$
		Other	
Acceleration of gravity	g	9.8 m s^{-1}	
Grain bulk modulus	K_S	70 Gpa	*Crone and Wilcock* [2002]
Upflow pressure gradient	$\delta p/\delta z$	-3000 Pa m^{-1}	

[a] Average values along an adiabatic path between 25 and 35 MPa.
[b] At a seafloor pressure of 25 MPa.
[c] Mean of values for layer 2B and 2C.
[d] Obtained using the relationship for basic rocks.

size the importance of obtaining more extensive observations for future events.

2. Temperature Perturbation Model

[8] In the motivation for his cracking front model, *Lister* [1974, 1983] argued that the high heat flux of mid-ocean ridge hydrothermal systems could not be sustained in static systems. He argued that thermal contraction in the conductive boundary layer underlying a hydrothermal system would cause vertical cracks to propagate downward and thus allow the hydrothermal system to mine heat deep into the oceanic crust. On most fast- and intermediate-spreading-rate segments his arguments seem wrong because it is now known that the reaction zone there is confined above a steady state mid-crustal magma chamber [e.g., *Detrick et al.*, 1987]. Nevertheless, the basic premise underlying Lister's model still holds because some mechanism must be found to maintain a thin conductive boundary layer and the chemistry of hydrothermal fluids requires that the system continually access fresh rock [e.g., *Seyfried and Shanks*, 2004]. The most obvious means to accomplish this is through repeated cracking events that open new pathways into unfractured regions.

[9] Such cracking events are likely to lead to a jump in the temperature of fluids entering the upflow zone. The simplest model that can be used to predict how a jump in temperature at depth will affect outflow temperatures is to consider the conservation of energy for one-dimensional flow through a Darcy continuum

$$\frac{\partial T}{\partial t} = -\frac{c_f \rho_f}{c_r \rho_r} q \frac{\partial T}{\partial z} + \kappa \frac{\partial^2 2T}{\partial z^2}, \qquad (1)$$

where T is the temperature, t is time, z is the vertical coordinate, c is the heat capacity, ρ is the density, q is the Darcy velocity, κ is the thermal diffusivity of the fluid saturated rock and subscripts f and r indicate properties of the hydrothermal fluid and the fluid saturated porous medium, respectively. The Darcy velocity can be written

$$q = -\frac{k}{\mu} \frac{dp}{dz}, \qquad (2)$$

where k is the permeability, μ the fluid viscosity and p is the nonhydrostatic pressure. For timescales of a few days the conductive length scale, $\sqrt{\kappa t}$ is <1 m (Table 1) and so the right-hand term of equation (1) can be neglected for temperature

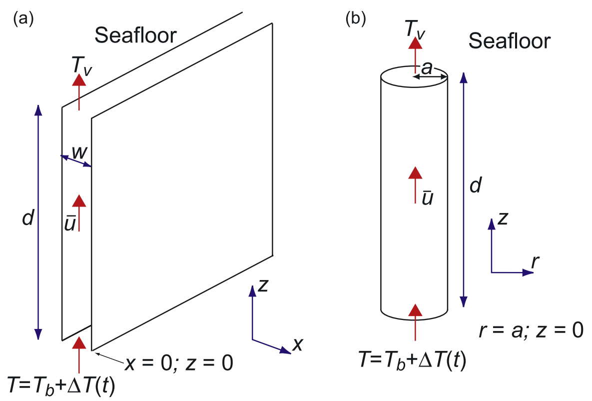

Figure 1. Schematic diagram showing the configuration of the upflow conduits used to model the effect of a temperature perturbation at the base of the upflow zone. (a) Hydrothermal upflow in a crack of width w has a mean velocity $\bar{u}$ and temperature T_b. A time-dependent temperature perturbation $\Delta T(t)$ is introduced to the fluids at a depth d, and the temperature response at the seafloor, T_v, is calculated. (b) As for Figure 1a except that the flow is through a pipe of radius a.

anomalies that are advected ~1 km over this time interval. The predicted venting temperature anomaly will mimic the temperature perturbation at depth except that it will be delayed by a time d/q where d is the depth of the perturbation. For a reasonable choice of properties (Table 1), equation (2) predicts that a permeability of $\sim 10^{-9}$ m^2 will be required to advect a temperature anomaly ~1 km in a few days. This is several orders of magnitude greater than the permeability commonly inferred for mid-ocean ridge systems [*Lowell and Germanovich*, 1994; *Wilcock and McNabb*, 1995].

[10] The reason for this discrepancy is that the continuum assumption of thermal equilibrium between the fluid and the entire rock matrix is inappropriate on short timescales. A more realistic model can be obtained by considering flow through a single conduit (or through a set of well-spaced conduits that are thermally isolated from one another) and explicitly accounting for heat exchange with the wall rock. I consider two simple end-member models for the geometry of the conduit (Figure 1); a planar crack of width w and a circular pipe of radius a. The second geometry not only simulates the flow that is likely to occur near the seafloor beneath discrete vents but may also approximate the flow in rough fractures where most of the flow is concentrated along a few pathways between regions where the crack walls are in contact or nearly so. I assume that the event changes the temperature of the fluids entering the base of the conduit. The hydrothermal fluids are well mixed within the conduit and flow at a mean speed $\bar{u}$. By balancing rate of heat exchange with the surrounding rock and heat advection up the conduit, I seek solutions for the temperature further up the conduit and hence for the temperature response at the seafloor.

2.1. Periodic Temperature Perturbations

[11] I first consider the response of the two geometries to a periodic temperature perturbation of amplitude ΔT and angular frequency ω introduced at the base of the conduit

$$T = T_b + \Delta T \cos \omega t, \tag{3}$$

where T_b is the temperature at the base of the conduit. Such solutions provide insights into the basic behavior of the model and form the basis for more complex solutions constructed using Fourier techniques.

2.1.1. Crack Geometry

[12] Assuming that the temperature perturbations in the conduit lead to negligible vertical heat conduction, the solution for the horizontal temperature structure in the rock at the base of the conduit is the response of a half-space to a periodic temperature variation at its surface [e.g., *Turcotte and Schubert*, 1982].

$$T_{z=0} = T_b + \Delta T \exp\left(-x\sqrt{\frac{\omega}{2\kappa}}\right) \cos\left(\omega t - x\sqrt{\frac{\omega}{2\kappa}}\right). \tag{4}$$

To calculate the temperature at higher levels, I balance the heat conducted horizontally out of the conduit with the heat flux up the crack according to

$$2\lambda\left(\frac{\partial T}{\partial x}\right)_{x=0} - \bar{u} w c_f \rho_f \left(\frac{\partial T}{\partial z}\right)_{x=0} = 0, \tag{5}$$

where λ is the thermal conductivity of the rock. In this expression I have neglected temporal variations in the heat content of the crack, an approximation that is valid provided $\kappa \gg \omega\, w^2$.

[13] The solution to the heat conduction equation which satisfies equations (4) and (5) is

$$T = T_b + \Delta T \exp\left(-x\sqrt{\frac{\omega}{2\kappa}}\right) \exp\left(-\frac{z}{H}\right) \cdot \cos\left(\omega t - x\sqrt{\frac{\omega}{2\kappa}} - \frac{z}{H}\right), \tag{6}$$

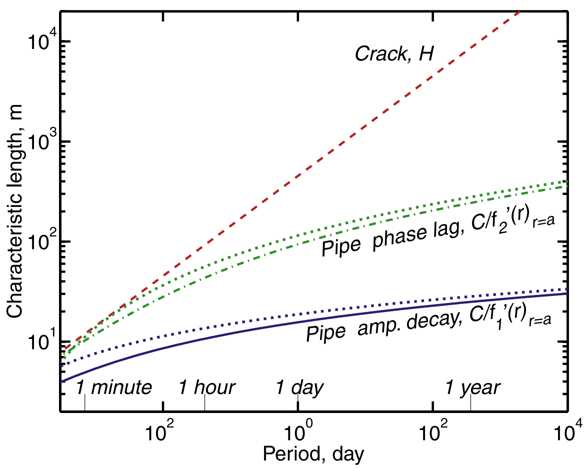

Figure 2. Characteristic length scale versus period for the attenuation and phase lag of a periodic temperature signal introduced at the base of a crack and pipe in the upflow zone. The calculations are for fluid fluxes that are equivalent to laminar flow through a crack of width 1 mm and a pipe of radius 0.87 mm; this radius has been chosen so that the fluid flux per unit horizontal length of conduit wall is the same for the two geometries. For a crack the characteristic length scale, H (red dashed line), is the same for the amplitude decay and phase lag. For a pipe the length scale for attenuation, $C/f_1'(r)_{r=a}$ (blue solid line), is markedly smaller than the length scale for the phase lag, $C/f_2'(r)_{r=a}$ (green dot-dashed line). The two dotted lines show the long-period approximations (equations (21) and (22)).

where H is a characteristic length scale for both the amplitude decay and phase delay and is

$$H = \sqrt{\frac{\kappa}{2\omega}\frac{\rho_f c_f \bar{u} w}{\lambda}}. \tag{7}$$

It is straightforward to show that the initial assumption of negligible vertical conduction is valid provided $\omega H^2 \gg \kappa$.

[14] For laminar flow, the mean velocity in the conduit is [e.g., *Turcotte and Schubert*, 1982]

$$\bar{u} = -\frac{w^2}{12\mu}\frac{dp}{dz}, \tag{8}$$

which leads to an alternative expression

$$H = -\sqrt{\frac{\kappa}{2\omega}\frac{\rho_f c_f w^3}{12\lambda\mu}\frac{dp}{dz}}. \tag{9}$$

Figure 2 shows this characteristic length plotted against the period of the temperature perturbations for a crack of width 1 mm assuming the fluid and rock properties given in Table 1. It increases from $\sim$10 m for periods of 1 minute to $\sim$500 m for periods of 1 day.

2.1.2. Pipe Geometry

[15] Proceeding along similar lines for the cylindrical conduit, the temperature in the rock at the base of the conduit is given by [*Carlslaw and Jaeger*, 1938]

$$T_{z=0} = T_b + \Delta T[f_1(r)\cos\omega t + f_2(r)\sin\omega t] \tag{10}$$

with

$$f_1(r) = \frac{\left(\ker\sqrt{\tfrac{\omega}{\kappa}}r\ker\sqrt{\tfrac{\omega}{\kappa}}a + \mathrm{kei}\sqrt{\tfrac{\omega}{\kappa}}r\,\mathrm{kei}\sqrt{\tfrac{\omega}{\kappa}}a\right)}{\ker^2\sqrt{\tfrac{\omega}{\kappa}}a + \mathrm{kei}^2\sqrt{\tfrac{\omega}{\kappa}}a} \tag{11}$$

$$f_2(r) = \frac{\left(\ker\sqrt{\tfrac{\omega}{\kappa}}r\,\mathrm{kei}\sqrt{\tfrac{\omega}{\kappa}}a + \mathrm{kei}\sqrt{\tfrac{\omega}{\kappa}}r\ker\sqrt{\tfrac{\omega}{\kappa}}a\right)}{\ker^2\sqrt{\tfrac{\omega}{\kappa}}a + \mathrm{kei}^2\sqrt{\tfrac{\omega}{\kappa}}a}. \tag{12}$$

The functions ker and kei are related to the zero order modified Bessel function of the second kind K_0 by

$$\begin{aligned}\ker z + i\,\mathrm{kei}\,z &= K_0\left[z\exp\left(\frac{i\pi}{4}\right)\right]\\ \ker z - i\,\mathrm{kei}\,z &= K_0\left[-z\exp\left(\frac{i\pi}{4}\right)\right]\end{aligned}. \tag{13}$$

For this geometry the balance of vertical heat advection in the conduit and horizontal heat loss can be expressed as

$$2\lambda\left(\frac{\partial T}{\partial r}\right)_{r=a} - \bar{u}ac_f\rho_f\left(\frac{\partial T}{\partial z}\right)_{r=a} = 0, \tag{14}$$

where I have again neglected changes in the heat content of the pipe (i.e., assumed $\kappa \gg \omega\, a^2$).

[16] The solution to equation (14) that satisfies equation (10) is given by

$$T = T_b + \Delta T\zeta(z)[f_1(r)\cos(\omega t - \eta(z)) + f_2(r)\sin(\omega t - \eta(z))], \tag{15}$$

where

$$\zeta(z) = \exp\left(\frac{f_1'(r)_{r=a}z}{C}\right), \tag{16}$$

$$\eta(z) = \frac{f_2'(r)_{r=a}z}{C}. \tag{17}$$

The terms $f'_1(r)_{r=a}$ and $f'_2(r)_{r=a}$ are derivatives of f_1 and f_2 with respect to r evaluated at a. The term C has units of length and is given by

$$C = \frac{\rho_f c_f \bar{u} a}{2\lambda}. \tag{18}$$

[17] For laminar flow, the mean velocity up a pipe [e.g., *Turcotte and Schubert*, 1982] is

$$\bar{u} = -\frac{a^2}{8\mu}\frac{dp}{dx}, \tag{19}$$

which yields an alternative expression:

$$C = -\frac{\rho_f c_f a^3}{16k\mu}\frac{dp}{dx}. \tag{20}$$

[18] The terms $C/f'_1(r)_{r=a}$ and $C/f'_2(r)_{r=a}$ are the characteristic length scales of the amplitude decay and phase delay of the temperature anomaly up the pipe. They are shown in Figure 2 assuming laminar flow through a cylinder of radius of 0.87 mm, a value that has been chosen because it has the same fluid flux per unit horizontal length of the conduit wall as laminar flow in a 1-mm-wide crack. Except at very short periods the characteristic length for the amplitude decay is substantially smaller than that for crack geometry. In contrast to the crack geometry, the length scale for the phase lag is not the same as that for the amplitude decay and is markedly smaller at all periods of interest. The physical implication is that the amplitude of any temperature perturbation traveling up a pipe will decay to a very small value before there is a significant phase lag.

[19] It is also apparent from Figure 2 that the characteristic lengths for the pipe geometry are only weakly dependent on the period of the perturbation. For example the characteristic length of the amplitude decay increases from 5 m at 1 hour to just 15 m at 1 day. The form of this weak dependency can be understood by using the series expansions of the Bessel functions [*Arfken*, 1985] to write first-order approximations for $f'_1(r)_{r=a}$ and $f'_2(r)_{r=a}$ under the assumption $a \ll \sqrt{\kappa/\omega}$:

$$\frac{C}{f'_1(r)_{r=a}} \sim -\frac{C}{a\ln\left(\frac{a^2\sqrt{\omega}}{4\kappa}\right)}, \tag{21}$$

$$\frac{C}{f'_2(r)_{r=a}} \sim -\frac{C}{2a\ln^2\left(\frac{a}{2}\sqrt{\frac{\omega}{\kappa}}\right)}. \tag{22}$$

These terms are only dependent on the logarithm of $\sqrt{\omega}$ while the term H for the crack geometry is dependent on $\sqrt{\omega}$ (equation (7)). The physical implication is that for perturbations that are generated sufficiently deep, there may be no observable signal at the seafloor even if they are sustained for a long time (one will never get hot water on the top floor of the hotel however long the tap runs). This may seem counterintuitive but can be understood by considering the cross-sectional area of rock that exchanges heat with the pipe. The conductive length scale varies as $\sqrt{\kappa t}$. Thus, for a perturbation of period t_p the pipe will exchange heat with a rock cylinder of radius $\sim\sqrt{\kappa t_p}$. Since the cross-sectional area of a cylinder is proportional to the radius squared, the volume of rock that is thermally coupled to the pipe increases linearly with t_p (as opposed to $\sqrt{t_p}$ for the crack geometry) and the walls efficiently absorb thermal perturbations, even for long period signals.

2.2. Step Change in Temperature

[20] In order to construct a simple model for the effects of a cracking event, I assume that the swarm leads to an instantaneous increase in the temperature of the fluids entering the upflow zone. The analytical solutions derived in the previous section can be summed to construct the response to a step increase in temperatures using Fourier methods. I calculate the Fourier transform of a 15-yearlong time series with a 1-hour sample interval (2^{17} samples) that has a step increase in temperatures 100 days before its end. I apply the solution of equations (6) or (15) to each component of the Fourier transform and then apply an inverse transform to obtain the predicted time series of vent temperatures. Because the Fourier transform assumes a periodic function, the solutions are strictly those for a 100-day-long temperature increase that occurs every 15 years. This results in a small offset in the temperatures just prior to the event. However, solutions obtained with time series for longer intervals show that after correcting for this offset, the earlier temperature events have a negligible effect on nondimensionalized solutions.

[21] Figure 3a shows predicted vent temperature time series for a 1-mm wide crack as a function of the height of the crack. For heights up to 1 km, the temperatures at the seafloor start to rise soon after the event and reach values that are close to the basal temperatures after 20 days. For larger heights, there is an appreciable delay in the response and the temperatures are still rising significantly after 20 days. The curves of Figure 3a can also be interpreted as the predicted vent temperatures for a 1-km-high crack as a function of crack width. The

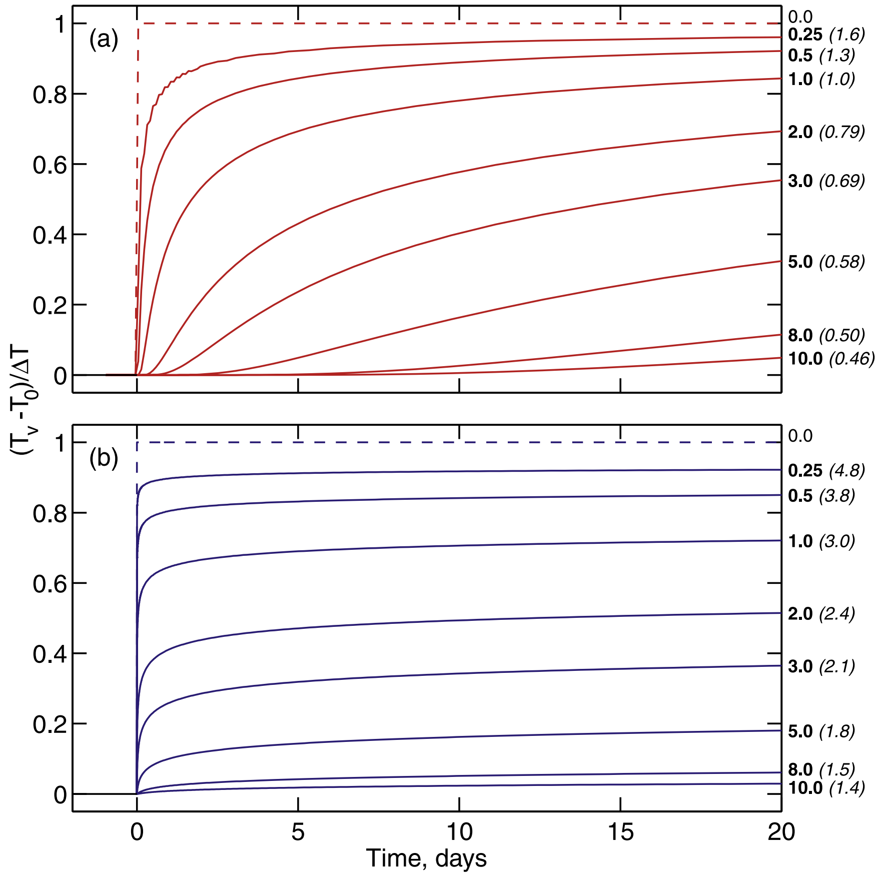

Figure 3. (a) Predicted time series of nondimensional vent temperatures, $(T_v - T_0)/\Delta T$, for the crack geometry. The curves can be viewed either as the predictions for cracks of different heights (labeled in bold in units of kilometers) assuming that the crack transports a fluid flux that is equivalent to laminar flow in a 1-mm-wide crack or as the predictions for a 1-km-high crack for fluid fluxes that are equivalent to laminar flow through cracks of various widths (labeled in parentheses in units of millimeters). (b) As for Figure 3a except for a pipe of radius 3 mm.

response becomes progressively delayed as the crack narrows.

[22] Figure 3b shows equivalent solutions for a pipe of radius 3 mm. The response is markedly different from the crack model. As the height of the conduit increases or equivalently its radius decreases, the amplitude of the observed response decreases but the temperatures at the seafloor always increase most rapidly soon after the causative event.

3. Pressure Perturbation Models

[23] There are several mechanisms whereby a sizable earthquake or magmatic intrusion might perturb the pressures within a mid-ocean ridge hydrothermal system. In this section, I discuss the mechanisms and consider how the diffusive response to such perturbations will modify hydrothermal outflow at the seafloor. I develop models for a Darcy continuum but completely equivalent models can be obtained for flow through individual cracks or a cracked medium provided it satisfies Darcy's law.

3.1. Transient Pressure Increase

3.1.1. Porosity Reduction

[24] One means to temporarily increase pressures at depth is to reduce the porosity (Figure 4a). In the dilatancy model for earthquake rupture [*Nur*, 1972; *Aggarwal et al.*, 1973] the region surrounding the fault dilates slowly prior to rupture in response to rising shear stresses that open fractures normal to the least compressive stress. On failure, the shear stresses are partially relieved, the fractures close and fluid pressures increase. *Sibson et al.* [1975] argue that this mechanism plays an important role in pumping hydrothermal fluids along many faults.

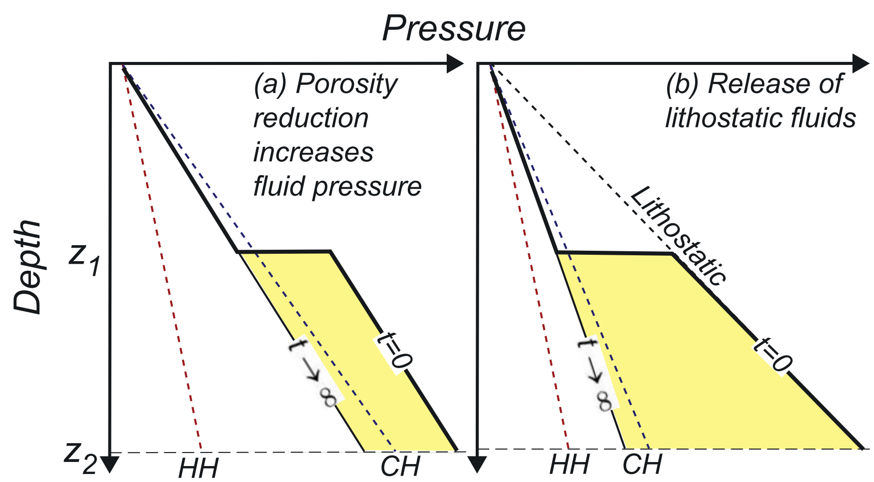

Figure 4. Schematic diagrams illustrating mechanisms by which a geological event can generate transient pressure increases that lead to increased outflow. The labels CH and HH indicate cold hydrostatic and hot hydrostatic gradients, respectively. The lines labeled $t = 0$ and $t \rightarrow \infty$ indicate the pressure distribution immediately after the event and a long time after the event, respectively. The yellow shaded regions show the excess pressures that will drive increased outflow immediately following the event. (a) A geological event relieves extensional strains, causing the porosity to decrease and the fluid pressures to increase at depths between z_1 and z_2. (b) A geological event opens a pathway that releases a reservoir of fluid at lithostatic pressures.

[25] However, for the normal faulting earthquakes expected on mid-ocean ridges, there is no need to invoke the dilatancy model to generate increased pressures. *Muir-Wood and King* [1993] looked at several major normal fault earthquakes in continental settings and show that each is followed by increases in spring and river discharges that peaked within days and persisted for up to a year. In contrast, reverse faulting earthquakes had no observable effects or led to decreased water levels and spring flows while strike slip faults had mixed and markedly smaller effects. *Muir-Wood and King* [1993] argue that for normal faults the interseismic period is associated with the opening of cracks normal to the direction of extension. At the time of the earthquake the cracks close and the water is expelled. For reverse faults the cycle is the opposite and the cracks open when compressive stresses are relieved.

[26] To explain the observations, *Muir-Wood and King* [1993] infer that closely-spaced vertical cracks are ubiquitous in continental crust although there is actually no actual need to invoke this particular pore geometry to explain the expulsion of fluids. The increase in fluid pressure, Δp, that results from a change in the normal stresses σ_{ii} can be written for any poroelastic medium [e.g., *Roeloffs*, 1996; *Wang*, 2000]

$$\Delta p = B\frac{\sigma_{ii}}{3}, \tag{23}$$

where B is Skempton's coefficient and is given by

$$B = \left(1 - \frac{K}{K_s}\right) \Big/ \left[1 - \frac{K}{K_s} + \phi K\left(\frac{1}{K_f} - \frac{1}{K_\phi}\right)\right], \tag{24}$$

where K is the drained bulk modulus of the fluid saturated porous medium, K_s is the unjacketed bulk modulus which can be equated to the bulk modulus of the solid grains, K_f is the fluid bulk modulus, K_ϕ is the unjacketed pore bulk modulus, and ϕ is the porosity. I assume that $K_\phi = K_s$ which is valid for a solid phase composed of a single constituent [*Wang*, 2000]. Taking reasonable properties of the lower part of the upper oceanic crust (i.e., seismic layers 2B/C) (Table 1) yields B = 0.3 and 0.03 for cold and hot hydrothermal fluids, respectively. These values are lower than the values of 0.5–1.0 typically observed for many fluid saturated rocks but are compatible with a value of 0.12 reported for Hanford basalt [*Wang*, 2000, p. 65 and Table C1]. However, my values may be significantly underestimated since $K_\phi < K_s$ for some rock types [*Wang*, 2000, pp. 51–52].

[27] For a simple plane-strain model of stresses on a normal fault [*Turcotte and Schubert*, 1982], the change in shear stress τ acting on the fault can be related to the mean normal stress by

$$\frac{\sigma_{ii}}{3} = \tau(1 + \nu)\cos\theta\sin\theta, \tag{25}$$

where ν is Poisson's ratio and θ is the dip of the fault. For a dip of 60°, $\tau \approx \sigma_{ii}/3$ and we can infer from equation (23) that a typical coseismic stress drop of 0.1–10 MPa (1–100 bars) will lead to pressure increases at depth of 0.03–3 MPa and 0.003–0.3 MPa in regions of cold and hot fluid, respectively.

[28] Similar pressure increases can be expected for a diking event. Near the dike tips, the crust will be placed in extension but elsewhere the region to either side of the dike walls will be compressed. For long dikes a much larger volume of crust will be placed under compression than extension even if the dike does not reach the seafloor [e.g., *Curewitz and Karson*, 1998]. The maximum compressive stress perturbation is equal to the internal pressure of the magma and is typically taken to be between 2 and 10 MPa [*Rubin and Pollard*, 1987]. *Curewitz and Karson* [1998] suggest that a value near the upper end of this limit is most appropriate for mid-ocean ridges. Assuming plane-strain (i.e., $\sigma_{ii} = (1 + \nu)\sigma_{11}$), equation (23) predicts an increase in fluid pressure up to 1 and 0.1 MPa in regions of cold and hot fluids respectively. Heating adjacent to the dike will lead to much larger pressure increases but only within a very narrow region [*Lowell and Germanovich*, 1995].

[29] For both earthquakes and diking events, significant stress induced pressure perturbations will extend out to distances similar to the minimum dimension of the fault plane [e.g., *Muir-Wood and King*, 1993] or dike [e.g., *Curewitz and Karson*, 1998]. Larger pressures increases in the cold fluid will act to drive fluid into the hot upflow zone where they will sustain a smaller pressure increase that will drive enhanced outflow. A complete model of the effect of such subsurface pressure perturbations would require a good understanding of the event geometry and three-dimensional solutions of the equations for flow within a poroelastic medium. However, basic insights into the likely response at the seafloor can be gained from a simplified one-dimensional model [*Muir-Wood and King*, 1993]. If one assumes that the coupling of the hydrological response to the deformation of the matrix is negligible after the coseismic stage, the evolution of the pressure perturbations are described in a one-dimensional Darcy medium (or completely equivalently for flow through fluid-filled fractures [*Muir-Wood and King*, 1993]) by a diffusion equation

$$\frac{\partial p}{\partial t} = \frac{k}{\mu S}\frac{\partial^2 p}{\partial z^2}, \tag{26}$$

where the specific storage S is a measure of the volume of fluid added per unit bulk volume for a unit increase in pressure. The full expression for S is quite complex but here for simplicity I assume that

$$S = \frac{\phi}{K_f}, \tag{27}$$

an approximation that is appropriate at larger depths where the drained bulk modulus approaches the grain bulk modulus and/or when the fluids are very compressible [*Wang*, 2000].

[30] I seek solutions to equation (26) for the evolution of a one-dimensional pressure perturbation for a model with an open upper boundary and a sealed lower boundary. These can be obtained analytically to yield a convergent sine series [*Carlslaw and Jaeger*, 1959] but I chose to use an explicit finite difference technique. Figure 5a shows the evolution of a pressure perturbation for a model with hot fluid (Table 1) and a permeability of 3×10^{-14} m^2 in which the pressure increases by 1 MPa between 1 and 2 km depth. The results for pressure perturbations other than 1 MPa can be obtained by linearly scaling the results. Figure 5b shows the volumetric outflow flux, q, as a function of time for a range of permeabilities and normalized to the outflow prior to the event, q_0 driven by a pressure gradient of 3 kPa m^{-1} in the upflow zone. The predicted fractional increase in outflow is quite small and its maximum value is independent of the permeability. As the permeability is decreased the system responds more slowly. For a permeability of 10^{-12} m^2 the outflow peaks in a matter of hours and decays back to initial values within ~5 days while for a permeability of 10^{-14} m^2, there is little change in flow for several days and the flow is still increasing after 20 days.

[31] Figure 6 shows a series of solutions for hot fluids and a permeability of 3×10^{-14} m^2 in which the depth and thicknesses of the pressurized layer are varied. Decreasing the depth of the pressurized layer (Figure 6a) results in a more peaked response which achieves higher maximum outflows and decays more rapidly. The effect of decreasing the thickness of the pressurized layer (Figure 6b) is to decrease the amplitude of the response. Increasing the thickness of the pressurized layer to values greater than its depth does not increase the peak outflow substantially but leads to a longer-lived response.

3.1.2. Release of High-Pressure Fluids

[32] Another mechanism to increase pressures at depth is to release a reservoir of high-pressure

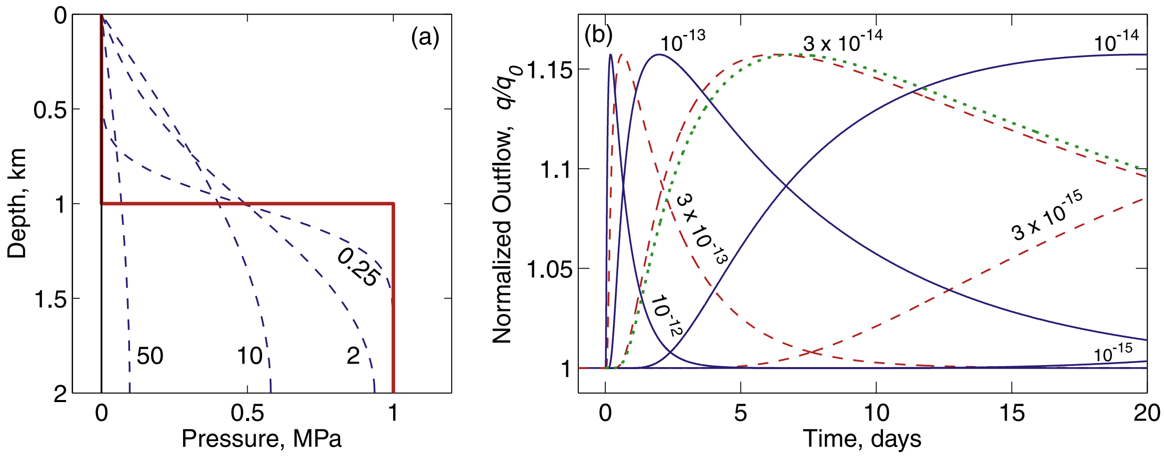

Figure 5. Results of one-dimensional calculations for the evolution of pressures for a starting model in which a 1 MPa pressure perturbation is applied to a 1-km-thick layer at 1 km depth (i.e., Figure 4a). (a) Initial (red solid) and final (black faint solid) vertical pressure profiles and the transient profiles at 0.25, 2, 10, and 50 days (blue dashed) for a permeability of 3×10^{-14} m^2. (b) Predicted fluid discharge (or pressure gradients) at the seafloor normalized to the discharge that would be driven by a pre-event pressure gradient of 3 kPa m^{-1} for models with permeabilities ranging from 10^{-12} to 10^{-15} m^2 (labeled blue solid and red dashed lines). The green dotted line shows the form of the curve for a loading model of the type shown in Figure 4b for a permeability of 3×10^{-14} m^2. The solution was obtained using an explicit finite difference technique with a 101 point grid and a time step that was 0.99 times that defined by the Von Neumann stability criterion (i.e., $\delta z^2 \mu S/4K$, where δz is the grid spacing).

fluids (Figure 4b). Hydrothermal alteration and precipitation will act to seal fractures and one feasible consequence of this process is the formation of isolated fluid reservoirs whose pressure will evolve over time toward lithostatic. If a fracturing event opens a pathway into such a reservoir, these high-pressure fluids will be released into the hydrothermal system. The maximum amplitude of the pressure pulse will be the difference between lithostatic and hydrostatic pressures

$$\Delta p = \left(\rho_r - \rho_f\right) g d, \tag{28}$$

where g is the acceleration of gravity. For the parameter values listed in Table 1 this equation predicts a maximum pressure increase of ~20 MPa at 1 km depth. This pressure perturbation is much larger than that predicted for a stress-induced change in porosity but it is likely that the source volume will be much smaller which would reduce the amplitude of the outflow response at the seafloor (i.e., the curves for 0.1 and 0.2 km pressurized layers in Figure 6b). Although the magnitude of the pressure perturbation increases with depth (Figure 4b) the form of the seafloor response (dotted green line in Figure 5b) is quite similar to that for a constant pressure perturbation.

3.2. Permeability Increase

[33] A dike intrusion or earthquake may substantially change the permeability structure within a hydrothermal cell both by creating fresh fractures and by opening and closing existing fractures in the modified stress field. If the relative flow resistance of the upflow and downflow zones changes, mass balance considerations require that the pressures in the system and/or the pattern of flow change. In the short term, pressure changes are likely to dominate because the thermal inertia of the rock matrix will inhibit a large scale reorganization of flow. It is generally accepted that vigorously convecting hydrothermal systems are at pressures close to cold hydrostatic because large pressure gradients are required to drive flow through a narrow upflow zone. In discussing the formation of event plumes *Wilcock* [1998] pointed out that a large increase in the permeability of the upflow zone would lead to increased pressure gradients driving downflow and the system would thus depressurize toward hot hydrostatic (Figure 7a).

[34] Figure 8a shows a one-dimensional calculation for the change in normalized outflow that would result from a uniform ninefold increase in permeability in a 2-km-high system where the initial resistance to upflow is 3 times that to downflow. Outflow peaks immediately following the change in permeability and then declines to the new equilibrium value at a rate that is proportional to the permeability.

[35] The peak response at the seafloor can be delayed if the increase in upflow permeability

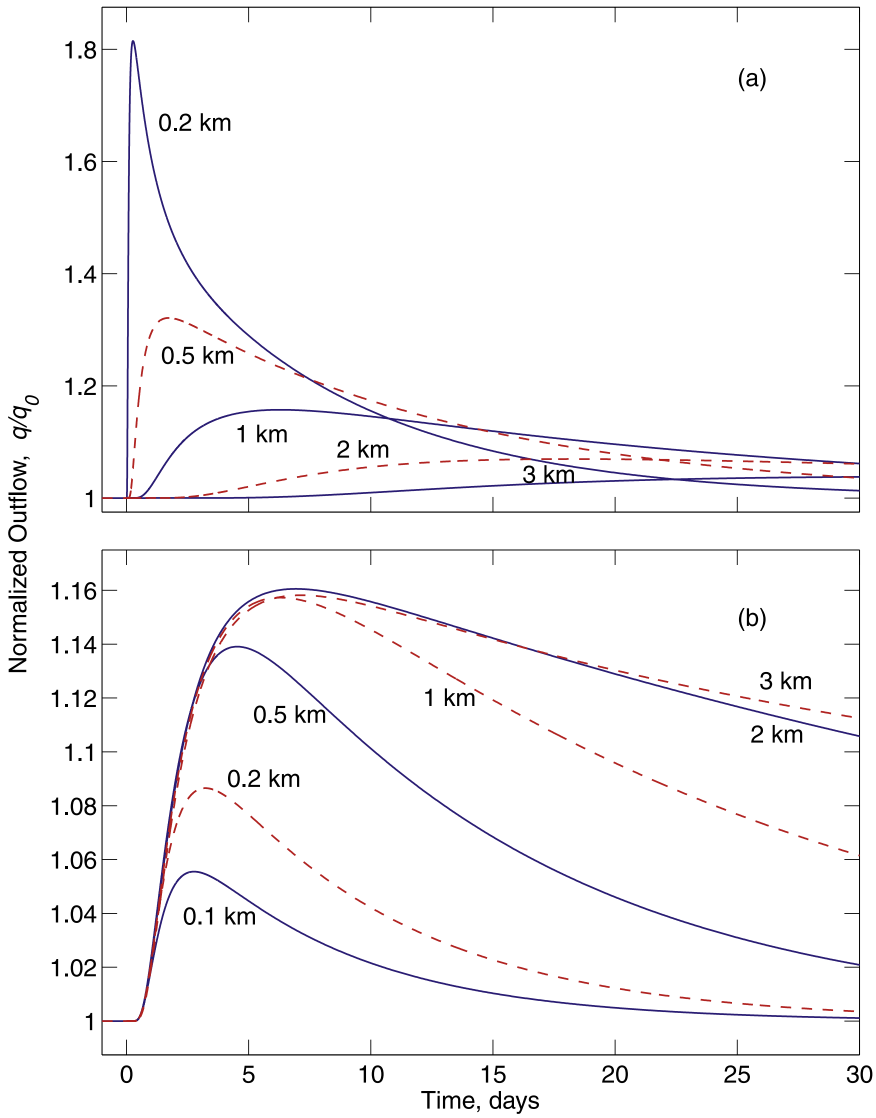

Figure 6. Effect on normalized discharge of changing the thickness and depth of a 1 MPa pressure perturbation of the type shown in Figure 4a for a permeability of 3×10^{-14} m^2. (a) The pressure perturbation is applied to a 1-km-thick layer at various depths (blue solid and red dashed lines labeled in kilometers). (b) The depth of the pressure perturbation is held at 1 km, and the thickness of the perturbed layer (labeled in kilometers) is varied.

occurs only at depth (Figure 7b) and is best illustrated by a simple example. The sum of the magnitude of the pressure gradients available to drive upflow and downflow is equal to the difference in cold and hot hydrostatic gradients, $g(\rho_h - \rho_c)$, where subscripts h and c refer to hot and cold hydrothermal fluid, respectively. It has a value of is 4 kPa m^{-1} for the properties listed in Table 1. One can define the flow resistance R of the upflow or downflow zone as

$$R = \int_0^d \frac{\mu}{kA} dz, \qquad (29)$$

where A is the cross-sectional area and d is the vertical extent. If the initial flow resistance of the upflow zone is 3 times that of the downflow zone, the pressure gradients driving upflow and downflow will be 3 kPa m^{-1} and 1 kPa m^{-1}, respectively. If the permeability of the bottom half of the upflow zone increases by a factor of 9, it is straightforward to show that the total flow resistance of upflow and downflow zones decreases to two-thirds of its initial value. The flow through the systems will increase by a factor of 1.5, the new pressure gradient driving downflow will be 1.5 kPa m^{-1} and the pressure gradients driving flow in the lower and upper halves of the upflow zone will be 0.5 and 4.5 kPa m^{-1},

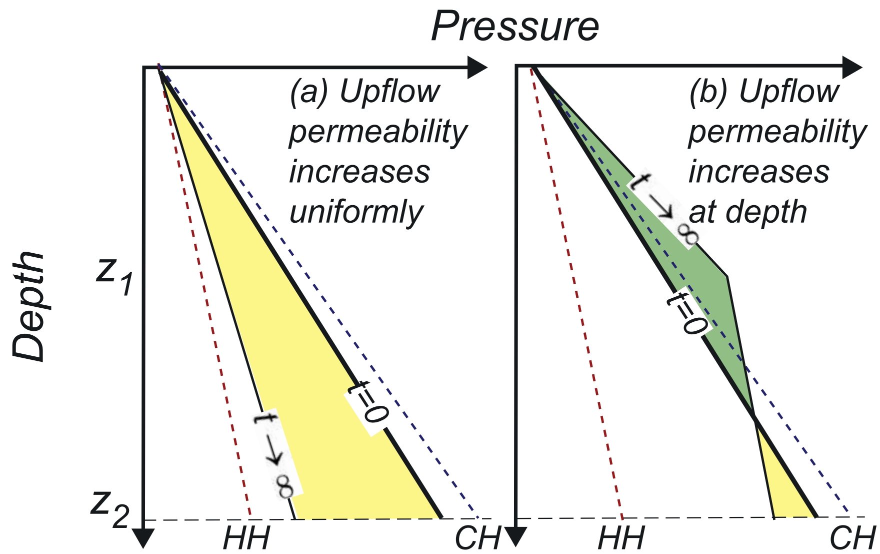

Figure 7. Schematic diagrams illustrating the mechanism by which increased permeabilities following a geological event can lead to increased outflow. The labels CH and HH indicate cold hydrostatic and hot hydrostatic gradients, respectively. The lines labeled $t = 0$ and $t \to \infty$ indicate the pressure distribution immediately after the event and a long time after the event, respectively. The yellow and green shaded regions show parts of the model that are overpressured and underpressured immediately following the event, respectively. (a) An increase in permeability throughout the upflow zone leads to a repartitioning of pressure gradients between the upflow and downflow zones and the pressure decay toward hot hydrostatic. (b) As for Figure 7a except that permeability increases only in the lower part of the upflow zone at depths between z_1 and z_2. If the flow resistance is still discharge dominated after the event, pressures will increase in the upper part of the upflow zone to drive increased outflow.

respectively. Since the system evolves to a configuration with higher pressure gradients driving outflow at the seafloor, the peak outflow will be equal to the final outflow but will be delayed by the diffusive response of the system.

[36] Figure 8b shows the predicted outflow for this example based on a one-dimensional numerical solution to equation (26) for the evolution of pressures in the upflow zone. The circulation depth is 2 km and solutions are presented for various choices of the initial permeability. For a permeability $\leq 10^{-13}$ m^2 the outflow rises to near its final value in a few days but for lower permeabilities the risetime is much slower and for permeabilities of 10^{-14} and 10^{-15} m^2 there is little change in outflow until $\sim$3 and $\sim$30 days, respectively. It is possible to generate substantially larger changes in outflow if the region of increased permeability extends closer to the seafloor (Figure 8c). For a given background permeability such a configuration leads to a faster response.

3.3. Effects of Pressure Perturbations on Venting Temperatures

[37] In the sections above, I have described models that lead to increases in the pressure gradients driving outflow at the seafloor and hence to increases in the outflow fluid fluxes. Increased outflow will very likely be accompanied by increased venting temperatures for both high-temperature and diffuse vents.

[38] For high-temperature vents, increased outflow may lead to increased venting temperatures because of decreased conductive cooling near the seafloor. If the rate of conductive heat loss from the hydrothermal conduit remains constant, the venting temperature T_v can be approximated by

$$T_v = T_{v0} + (T_u - T_{v0})\left(1 - {}^{q_0}/_{q}\right), \qquad (30)$$

where T_u is the fluid temperature at the base of the upflow zone, q is the outflow velocity (or volumetric flux) and the subscript 0 refers to values before the event. For simplicity, adiabatic gradients in the upflow conduit have been neglected and the expression assumes that the volumetric heat capacity of the fluid remains constant over the temperature range of interest. Figure 9a shows the results of applying equation (30) to the transient pressure increase solutions shown in Figure 5b assuming T_{v0} = 365°C and T_u = 385°C. These particular solutions predict an

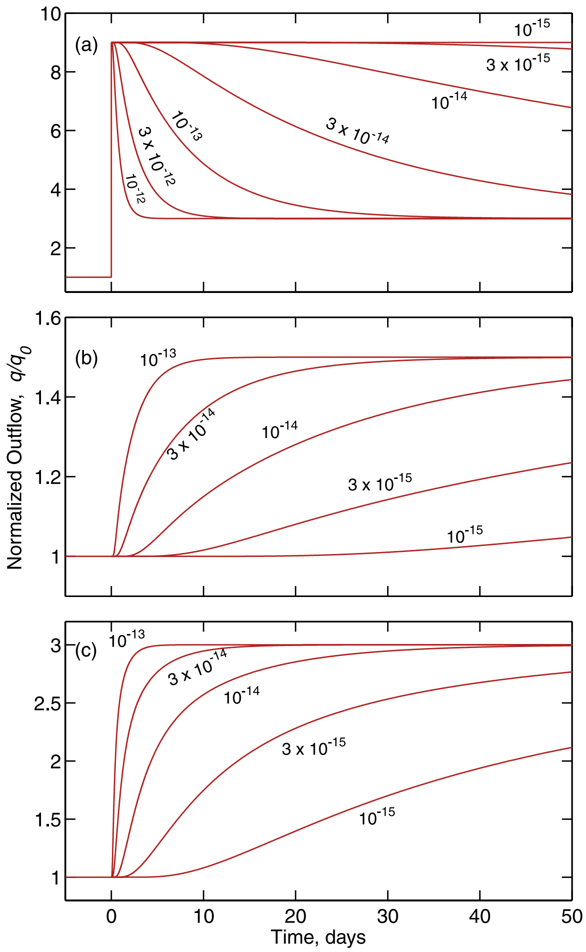

Figure 8. Normalized discharge velocities resulting from decreased permeabilities in the upflow zone. (a) The permeabilities decrease by a factor of 9 throughout a 2-km-high upflow zone. Prior to the event the pressure gradients driving upflow and downflow are 3 and 1 kPa/m, respectively, and well after the event they reverse, leading to a threefold increase in outflow. The transient response leads to a temporary ninefold increase in outflow that declines at a rate that is proportional to the permeability. Curves are shown for several different values of permeability (the labeled permeability is the permeability after the event just below the seafloor). (b) As for Figure 8a except that the permeabilities increase only in the lower 1 km of the upflow zone. After the event the outflow velocity increases at a rate that is proportional to the permeability to a final value that is 1.5 times the initial value. (c) As for Figure 8b except that the flow resistance of the downflow zone is negligible before and after the event and the permeabilities increase in the lower 1.5 km of the upflow zone. The final discharge velocities are 3 times the initial value.

increase in venting temperature of $\sim$3°C but the magnitude of this increase is dependent on both the magnitude of the pressure perturbations and the extent of conductive cooling before the event. Figure 9b shows the equivalent temperature predictions for the permeability increase model solutions of Figure 8b. The predicted increase in venting temperature is higher than for Figure 9a because q/q_0 is higher for these solutions.

[39] Diffuse vent fluids are formed by a mixture of a small component of a high-temperature end-member fluid and cold seawater. If the flux of cold seawater remains constant and is much greater than the flux of hot fluid, the change in venting temperature resulting from an increase in the volumetric flux q of the hot fluid can be approximated by

$$T_v = T_{v0} + (T_{v0} - T_c)\left({}^{q_0}/_{q} - 1\right), \quad (31)$$

where T_c is the temperature of the cold seawater component. Figure 9c shows the results of applying equation (31) to the solutions of Figure 5b assuming T_{v0} = 4°C and T_c = 2°C. The predicted temperature increases are quite small. However, the increase in the flux of high-temperature fluids entering diffuse vent sites may be much larger than the value q/q_0 predicted for the whole vent field. If the seismic event causes pressures in the upflow zone to increase and/or the cross-sectional area of the upflow zone to expand, there may be a very substantial increase in the proportion of high-temperature fluids that spill out around the margins of the upflow zone and mix with cold seawater to form diffuse outflow. A more appropriate expression for the change in venting temperature is

$$T_v = T_{v0} + (T_{v0} - T_c)\left(\frac{q_0}{[q_0 + \alpha(q - q_0)]} - 1\right), \quad (32)$$

where α is a constant that may be substantially larger than unity. Physically it is the fractional increase in the flux of the high-temperature component at the diffuse vent site normalized to the mean increase for the whole vent field. Figure 9d shows the result of applying equation (32) to the solutions of Figure 5b assuming T_{v0} = 4°C, T_c = 2°C and α = 10. Compared to Figure 9c, the increase in temperatures is amplified by a factor $\sim\alpha$.

4. The 1995 East Pacific Rise Event

[40] The temporal relationships for the East Pacific Rise event are summarized in Figure 10. The main earthquake swarm comprised just under 100 locatable earthquakes (162 in total) that occurred within a 3 hour interval on March 22, 1995. The earthquakes are clustered at a depth of $\sim$1 km and a

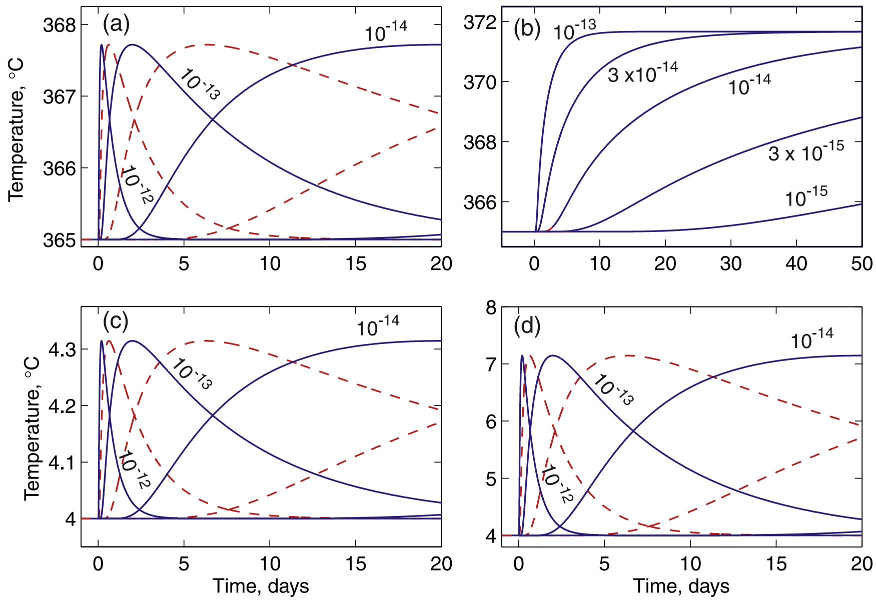

Figure 9. Examples of the temperature perturbations that are predicted for pressure perturbation models. (a) Temperatures predicted using equation (30) for a high-temperature vent for the transient pressure increase solutions shown in Figure 5b assuming T_{v0} = 365°C and T_u = 385°C. The labels indicate the permeabilities. (b) As for Figure 9a except that the temperatures are predicted for the permeability increase model of Figure 8b. (c) As for Figure 9a except that the temperature predictions are obtained with equation (31) for a diffuse vent assuming T_{v0} = 4°C and T_c = 2°C. (d) As for Figure 9a except that the temperature predictions are obtained with equation (32) for a diffuse vent assuming T_{v0} = 4°C, T_c = 2°C and α = 10.

relative relocation shows that they lie within a 300-m-high vertical column located a few hundred meters to the NNW of the Bio9 vent [*Sohn et al.*, 1998]. The polarity of the stacked waveforms are fit by an oblique normal faulting focal mechanism with an axis of minimum compressive stress oriented perpendicular to the rise axis [*Sohn et al.*, 1999].

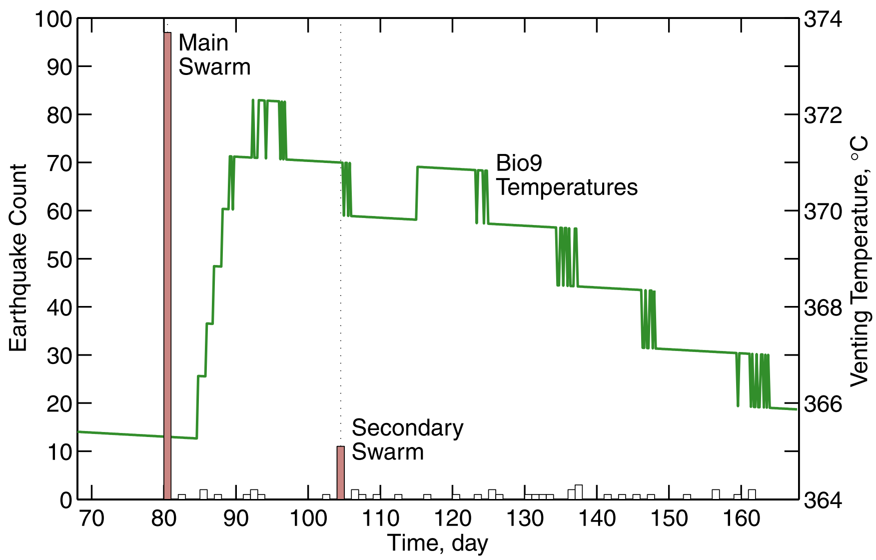

Figure 10. Summary of the 1995 cracking event on the East Pacific Rise near 9°50′N showing a histogram of the microearthquake count for locatable events in one day bins [*Sohn et al.*, 1998, 1999] and a time series of temperatures for the Bio9 vent [*Fornari et al.*, 1998]. Times are plotted in days relative to 00:00 GMT on January 1, 1995. Shaded regions of the histogram highlight two short swarms occurring 24 days apart that were located ~1.0 km beneath the Bio9 vent. The temperature measurements have a precision of 1.3°C, and a long-term linear trend of increasing temperatures has been removed from the data [*Fornari et al.*, 1998].

[41] For a year prior to the event the temperatures of Bio9 were very stable except for a long term trend of temperatures increasing steadily at ~3°C/year that continued well after the event [*Fornari et al.*, 1998]. Following the swarm, the temperature of the Bio9 vent remained steady at the pre-swarm temperatures of 365°C for 4 days and then started to increase sharply at a rate that initially exceeded 1°C/day [*Fornari et al.*, 1998]. The temperature peaked at 372°C 11–15 days after the swarm and then decreased over the next two months to just above pre-swarm levels. A second swarm of 11 locatable earthquakes (26 total) occurred 24 days after the first [*Sohn et al.*, 1998] and was followed 10 days later by a 1°C increase in vent temperatures that interrupted the otherwise steady decline. At other times, the earthquake count never exceeded 3 per day and nearly all of these nonswarm earthquakes were located about 1 km to the south of the Bio9 vent [*Sohn et al.*, 1999].

[42] This event is interpreted as a cracking event in which the earthquake swarms opened up a new pathway to hot rock at the base of the hydrothermal cell [*Fornari et al.*, 1998; *Sohn et al.*, 1998]. The chemistry of discrete fluid samples lends support to this model since the depth of the water/rock reaction zone appeared to deepen between October 1994 and November 1995 [*Sohn et al.*, 1998]. In order to test whether the cracking event model can fit the data, I first searched for models with a step increase in basal temperatures that matched the initial rise in temperature. It is clear from Figure 3b that the pipe geometry cannot reproduce the initial delay in risetime and thus I focused on the crack geometry and varied both the amplitude of the basal temperature jump and the crack width. The results (Figure 11) show that model can fit the data but only when the basal temperatures increase by ≥~50°C. For smaller temperature jumps (Figure 11a) the root mean square (RMS) misfit of the best fitting curve is much larger (Table 2) and it is not possible to fit both the 4 day delay and the rate of the subsequent temperature increase. For a temperature increase of 50°C (Figure 11b), the data are well fit by an effective crack width of 0.59 mm provided that the pre-swarm temperature is ~0.5°C cooler than the value recorded. This is compatible with the data because the digital resolution of the measurements is only 1.3°C. The data can also be fit well for larger temperature increases if the crack width is slightly narrower (Figures 11c and 11d).

[43] It is clear from Figure 11 that the basal temperatures must decline after their initial jump if the

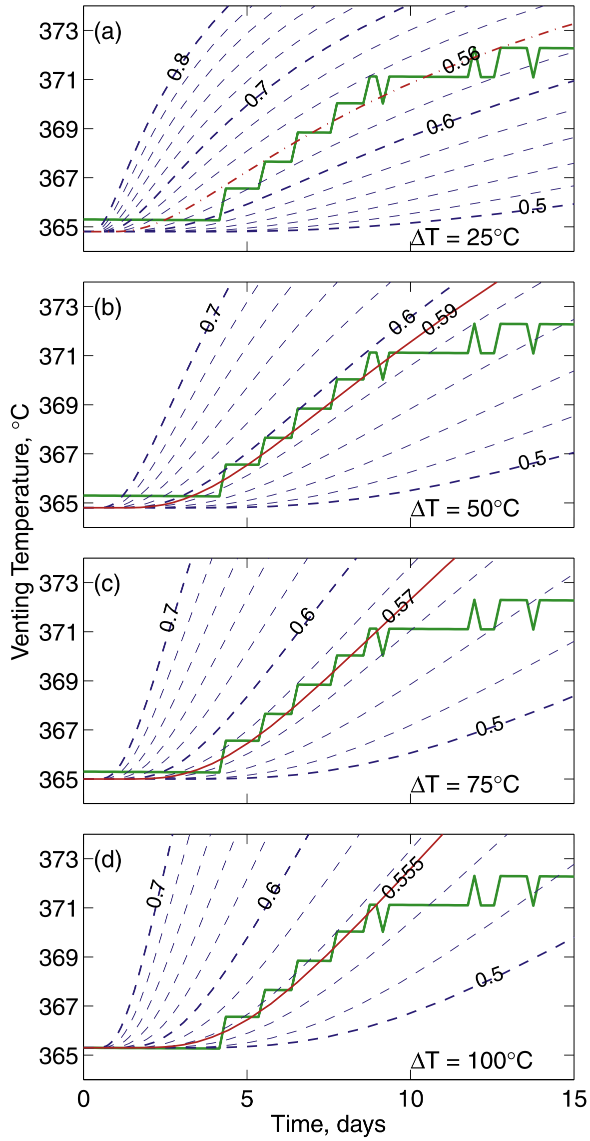

Figure 11. Temperature perturbation models for the initial increase in temperatures observed in the Bio9 vent on EPR near 9°50′N following the cracking event. Times are plotted relative to the first event in the earthquake swarm of March 22, 1995, and the field data with the long-term trend removed are shown as a green bold line. The blue dashed lines show solutions for a step increase in temperatures at time zero and at a depth of 1.1 km below the seafloor time zero for crack widths in 0.02 mm increments (bold and labeled every 0.1 mm) and temperature increases of (a) 25°C, (b) 50°C, (c) 75°C, and (d) 100°C. Solid red lines in Figures 11b–11d show solutions that fit the data well, and a dot-dashed red line shows the best fitting solution in Figure 11a. Note that the discretization interval of the field data is 1.3°C [*Fornari et al.*, 1998] and solutions for a temperature increase of 50 and 75°C fit the observations best if the initial temperature lies near the lower end of this interval.

Table 2. Model Misfits[a]

Figure	Line Type	Model Description	Model Parameters	Time Interval, days	RMS Misfit, °C
			East Pacific Rise		
11b	dot-dash red	temperature jump	w = 0.64 mm, ΔT = 25°C	0–10	0.75
11b	solid red		w = 0.59 mm, ΔT = 50°C	0–10	0.47
11c	solid red		w = 0.57 mm, ΔT = 75°C,	0–10	0.43
11d	solid red		w = 0.555 mm, ΔT = 100°C,	0–10	0.47
12	solid red	temperature jump and ramp down	w = 0.6 mm, ΔT = 50°C, Δt = 16 d	0–25	0.54
13	dot-dash blue	double temperature event	2nd event: w = 0.6 mm, ΔT = 24°C, Δt = 16 d	0–85	0.56
	solid red		2nd event: w = 0.6 mm, ΔT = 17°C, Δt = 25 d	0–85	0.44
	dotted black	two pressure jumps, 1–1.08 km	$k_0 = 5 \times 10^{-15}$ m^2; ΔP = 20 and 4 MPa, $T_u - T_{v0}$ = 19°C	0–85	0.55
			Endeavour–Easter Island		
15a	solid red	pressure jump, 1–2 km	Δp = 1 MPa, $k_0 = 3.5 \times 10^{-15}$ m^2, α = 14.5	0–14	0.069
				0–80	0.85
				0–80	0.93
	dot-dash blue	ninefold permeability jump, 0.5–2 km	$k_0 = 1.6 \times 10^{-15}$ m^2, α = 1.8	0–14	0.053
				0–80	0.87
16a	dash black	temperature step	w = 0.66 mm, $\varepsilon\Delta T$ = 10°C	0–14	0.058
				0–80	1.2
	dot-dash blue	temperature step	w = 0.62 mm, $\varepsilon\Delta T$ = 20°C	0–14	0.12
				0–80	2.8
	solid red	temperature jump and ramp down	w = 0.66 mm, $\varepsilon\Delta T$ = 10°C, Δt = 100 d	0–14	0.084
				0–80	0.83
			Endeavour–Beach		
15b	dotted black	pressure jump 1–2 km	Δp = 1 MPa, $k = 8 \times 10^{-15}$ m^2, α = 64	4-45	0.056
	solid red	pressure jump, 0.5–2 km	Δp = 1 MPa, $k = 5 \times 10^{-15}$ m^2, α = 9, Delay 4 d	4-45	0.052
	dashed black	ninefold permeability jump, 1–2 km	$k_0 = 2.5 \times 10^{-14}$ m^2, α = 7, Delay 8 d	8-45	0.048
	dot-dash blue	ninefold permeability jump, 0.5–2 km	$k_0 = 6 \times 10^{-15}$ m^2, α = 3, Delay 8 d	8-45	0.047
16b	dot-dash blue	temperature step	w = 0.89 mm, $\varepsilon\Delta T$ = 1.2°C, Delay 8.5 d	8.5–45	0.045
	dash black	temperature jump and ramp down	w = 0.71 mm, $\varepsilon\Delta T$ = 3°C, Δt = 60 d, Delay 4 d	4-45	0.063
	solid red	temperature jump and ramp down	w = 0.58 mm, $\varepsilon\Delta T$ = 80°C, Δt = 3 d	4-45	0.076

[a] The model description and model parameter entries provide a cryptic description of the models and a listing of some key parameters. For a complete description, refer to the figure captions and the text. The time interval listed is that used to calculate the RMS model misfit to the temperature data.

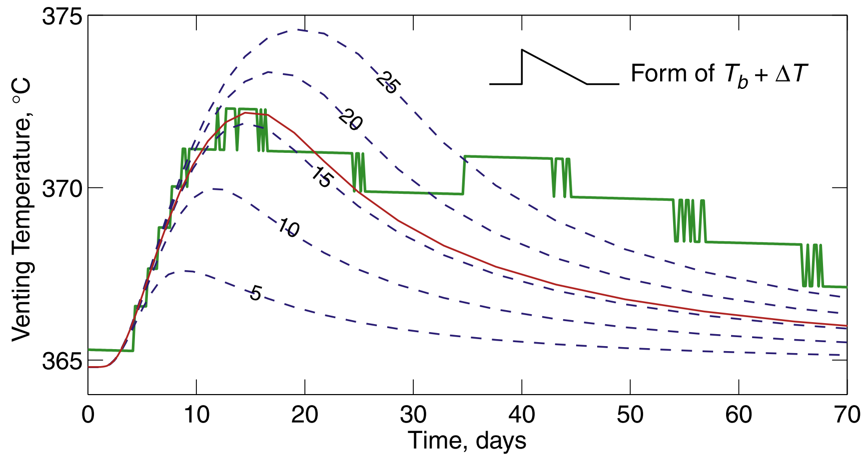

Figure 12. Single-event models for the temperatures observed at the Bio9 vent. Times are plotted relative to the first event in the earthquake swarm, and the field data are shown as a green bold line. Dashed blue lines show solutions for a 0.60-mm-wide crack assuming that the fluid temperature at 1.1 km depths increases by 50°C at time zero and then decays linearly back to its starting value over 5, 10, 15, 20, and 25 days. The red solid line shows a solution for a decay time of 16 days that fits the temperature data well for the first 25 days, but a second event is clearly required to fit the data at later times.

model is going to fit the temperature time series after ~10 days. This presumably occurs because the hydrothermal fluids cool the rock adjacent to the fractures that were opened by the cracking event. For simplicity I assumed that the basal temperature starts to ramp down linearly back to its initial values immediately after increasing and I sought to match the data by varying the time over which this occurs. Figure 12 shows solutions for a basal temperature jump of 50°C and a 0.60-mm-wide crack. The first 25 days of temperature data are fit well (Table 2) by a model in which the basal temperature anomaly declines back to its initial value over 16 days.

[44] To fit the remainder of the time series, I explored models in which a second smaller basal temperature jump occurred at the time of the secondary swarm (Figure 13). Assuming this second temperature jump also ramps down over 16 days,

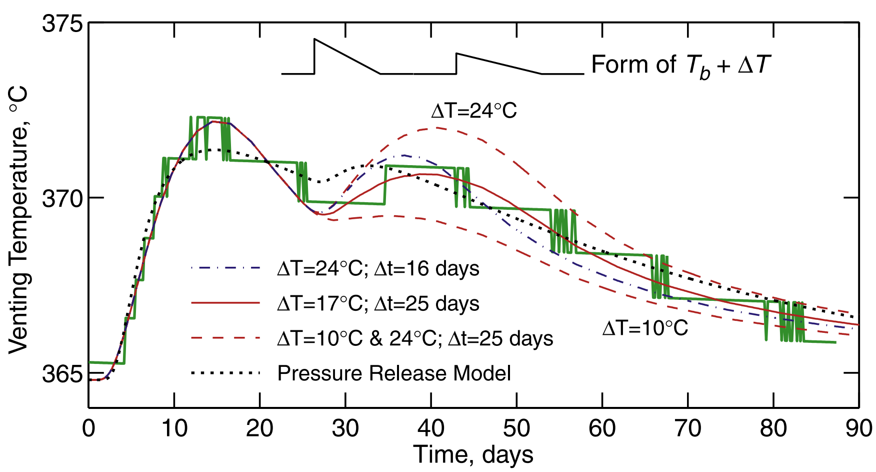

Figure 13. Double-event models for the temperatures observed at the Bio9 vent. Times are plotted relative to the first event in the earthquake swarm, and the field data are shown as a green bold line. The crack width is 0.6 mm, and the depth of the perturbation is 1.1 km. The initial event is modeled by a 50°C increase in temperature that decays linearly over 16 days. A second event 24 days later is modeled as a step increase of 24°C that decays over 16 days (blue dot-dashed line) and step increases of 10°C (red dashed line), 17°C (red solid line), and 24°C (red dashed line) that decay over 25 days. The dotted black line shows an attempt to fit the data with a pressure perturbation model using equation (30). The two swarms release the fluids in 80-m-thick layers at 1.1 km depth with excess pressures of 20 MPa and 4 MPa, respectively. The permeability $k = 5 \times 10^{-15}$ m^2, and the conductive cooling prior to the event $(T_u - T_{v0}) = 19$°C.

the best fit was obtained for an amplitude of about 24°C. However, a markedly better fit was obtained by increasing the ramp-down time to 25 days and decreasing the amplitude to 17°C (Table 2). Indeed this solution fits the whole time series within the discretization error of the measurements.

[45] One of the assumptions of the temperature perturbation model is that the flow occurs in isolated cracks that do not interact thermally. For timescales of 10 days the conductive length scale, $\sqrt{\kappa t}$, predicted for the properties listed in Table 1 is 0.7 m, so the assumption of thermally isolated cracks is probably valid provided the principal cracks carrying fluid flow are spaced at least 2 m apart. This is not a onerous requirement and, except perhaps near the very base of the circulation cell, is compatible with conceptual models of hydrothermal upflow [e.g., *Goldfarb and Delaney*, 1988].

[46] The models predict that a temperature jump of at least ~50°C is required in the reaction zone to reproduce the seafloor observations. The chemistry of discrete fluid samples collected from the Bio9 vent well before and after the event show clear evidence for phase separation [*Sohn et al.*, 1998] which requires that at least a component of the fluid circulated to ~430°C [*Anderko and Pitzer*, 1993]. Our model would suggest that either the proportion of fluid circulating near the two-phase curve increased substantially or that the maximum fluid temperatures increased well into the two phase region. Either process would have led to a substantial change in fluid chemistry during the event.

[47] For the predicted crack width of 0.6 mm and the fluid properties of Table 1, equation (6) yields a laminar flow velocity of 1.2 m/s. The Reynolds number for flow in a crack is $\bar{u}w\rho/\mu$ and the predicted value is ~3000. This is slightly higher than the values of ~1000 at which turbulent flow is observed in some laboratory experiments [*Carlson et al.*, 1982] but less than the transitional value of 5772 predicted from linear stability analysis [*Orszag*, 1971]. Since rough crack walls will favor turbulent flow, the flow is probably mildly turbulent. The actual effective width of the crack may be somewhat larger and the mean flow velocity smaller than predicted for laminar flow. One clear prediction of the model is that there must be a pathway from the reaction zone to the seafloor along which fluids move very rapidly; any chemical anomalies associated with a basal temperature increase would be detectable at the surface in less than an hour, provided the fluids do not reequilibrate chemically as they rise.

[48] The inferred fluid fluxes within a crack can also be used to estimate the likely spacing of the fractures. Equating the Darcy velocity q for flow through a Darcy medium and flow through parallel fractures spaced a distance L apart yields $q = \bar{u}w/L$. Models for the heat fluxes of high-temperature systems suggest that the permeability is $\sim 10^{-12}$–10^{-13} m^2 [*Lowell et al.*, 1995; *Wilcock and McNabb*, 1995]. Combining these values with those in Table 1 and making use of equation (2) yields a crack spacing of 20–200 m. This prediction is in reasonable agreement with other studies [*Nehlig*, 1994]. It is also compatible with the assumption that the main cracks transporting flow do not interact thermally.

[49] Since there are no hydrothermal flow measurements for the EPR event, one cannot entirely discount the possibility that a transient increase in outflow could have increased vent temperatures by reducing the effects of near surface conductive cooling. The reported moments of 10^7–10^9 Nm (10^{14}–10^{16} dyne-cm) [*Sohn et al.*, 1999] are equivalent to fault diameters of only 0.2–4 m [*Brune*, 1970] assuming typical earthquake stress drops for small earthquakes of 0.1–10 MPa (1–100 bar). Pressure perturbations in volumes of such small dimensions are unlikely to have had a significant effect at the seafloor. Small earthquakes could have a substantial effect on the flow resistance of a hydrothermal cell by fracturing a choke point of low permeability, but the EPR event did not lead to the permanent increase in vent temperatures predicted for this model (e.g., Figures 8b and 8c). It is possible that each swarm released a reservoir of high-pressure fluids although the permeability of $< 10^{-14}$ m^2 required to generate a 4 day delay (Figure 5b) is substantially smaller than typically inferred for high-temperature hydrothermal systems [*Lowell and Germanovich*, 1994; *Wilcock and McNabb*, 1995]. Figure 13 shows that such a model can fit the form of the temperature data reasonably well although not as well as the temperature perturbation model (Table 2).

5. The 1999 Endeavour Event

[50] The 1999 Endeavour event is summarized in Figure 14. In comparison to the 1995 EPR event, the relationships between the earthquakes and the temperature time series are poorly constrained. There was no local seismic network in place to

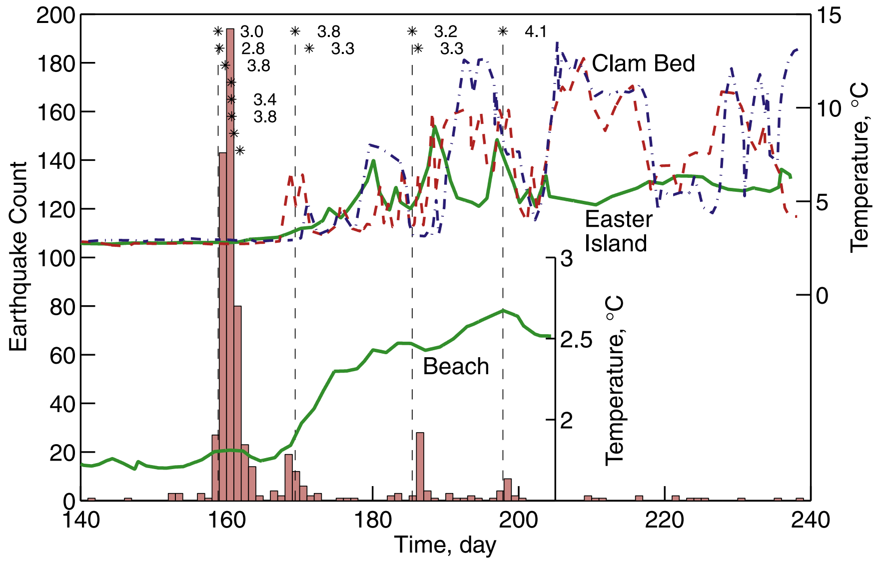

Figure 14. Summary of earthquake times and vent temperatures for the 1999 earthquake swarm on the Endeavour segment of the Juan de Fuca Ridge showing a histogram of the earthquake count for the SOSUS acoustic network [*Fox et al.*, 1994; *Johnson et al.*, 2000], earthquakes in the International Seismological Centre (ISC) catalog (International Seismological Centre, On-line Bulletin, Thatcham, UK, 2001; http://www.isc.ac.uk/Bulletin/rectang.htm), and smoothed temperature time series from four diffuse vent sites [*Johnson et al.*, 2000]. Times are plotted relative to 00:00 GMT on January 1, 1999. The histogram shows 625 earthquakes that are listed in the on-line SOSUS epicenter catalog for April 21, 1999, through August 28, 1999, for the latitude and longitude limits of 47.4°N–48.2°N and 128.8°W–129.8°W, respectively. Asterisks show the times of the 13 earthquakes in the ISC catalog, and where available these are labeled with surface wave magnitude calculated by ISC or Experimental International Data Center. The vertical dashed lines show the times of the first teleseismic earthquake in each interval of peak seismicity. The temperature time series are from the Beach site located 200 m south of the Main vent field (lower green solid line), the Easter Island site within the Main vent field (upper green solid line), and the Clam bed site near the High Rise vent field (red dashed and blue dot-dashed lines).

provide accurate locations and the timing of the causative earthquake(s) is uncertain because the swarm activity persisted for over a month. The SOSUS network detected ~2700 earthquakes [*Johnson et al.*, 2000; *Bohnenstiehl et al.*, 2002, 2004], of which ~600 located events are included in the on-line catalog (http://www.pmel.noaa.gov/vents/acoustics/seismicity/seismicity.html). Most of the SOSUS earthquakes occurred within 4–5 days of the swarm but significant activity within the region persisted for over 40 days with secondary peaks 10, 28 and 40 days after the main event. The majority of the SOSUS earthquake locations lie within a region centered near 47°50′N that extends about 30 km along the ridge axis and 25 km out onto the western flank [*Johnson et al.*, 2000] but there is also a significant concentration of seismicity 30 km to the southwest near Surveyor (Split) Seamount on the Cobb segment [*Bohnenstiehl et al.*, 2004]. The center of activity for earthquakes in the main grouping migrated southward over the first 1–2 days [*Bohnenstiehl et al.*, 2004] and the majority of earthquakes occurring later in the swarm are located south of 47°50′N. The median one standard deviation epicentral uncertainties for latitude and longitude are 2 km and 13 km [*Bohnenstiehl et al.*, 2004] and there may also be significant biases in the locations. For this reason the SOSUS epicenters are inadequate to identify with certainty earthquakes that occurred very near the vent fields.

[51] Thirteen earthquakes were large enough to be reported in the International Seismic Center catalog (International Seismological Centre, On-line Bulletin, Thatcham, UK, 2001; http://www.isc.ac.uk/Bull), including 1 or 2 earthquakes during each secondary peak in activity. The reported body wave and surface wave magnitudes range from 3.4–4.5 and 2.8–4.1, respectively, and moment tensor solutions for a subset of these events show both normal and strike-slip mechanisms with tension axes perpendicular or sub-perpendicular to the ridge axis [*Davis et al.*, 2001].

[52] Since the SOSUS locations are concentrated on the west flank of the ridge axis and the first earth-

quake was teleseismic, the swarm was originally interpreted as tectonic [*Johnson et al.*, 2000]. However, subsequent analysis showed that it had many characteristics of a volcanic swarm [*Bohnenstiehl et al.*, 2001, 2002]. Discrete fluid samples collected a few months after the event record a large increase in volcanic gas concentrations [*Lilley et al.*, 2003] and other chemical characteristics of the fluids are also indicative of magmatic influence [*Seyfried et al.*, 2003]. No evidence has been reported for an eruption but it is very likely the event was associated with a magmatic intrusion and one can infer that many, if not all, of the earthquakes occurred near the ridge axis.

[53] An intriguing aspect of the Endeavour earthquake swarm is that it led to hydrologic pressure transients that were measured in sealed Ocean Drilling Program boreholes up to 100 km away [*Davis et al.*, 2001]. Pressures rose coseismically with the first earthquake, continued to rise for several hours and then decayed on timescales of 1–2 days and 100 days at sites that were 30 km and 100 km away, respectively. *Davis et al.* [2001] show that the coseismic pressure change can be explained by the volumetric strain associated with 12-cm of extension on a plane extending to 3 km depth and 40 km along axis. The subsequent behavior of the pressure field can be modeled by two-dimensional hydrologic diffusion within a high-permeability basement layer (10^{-9} to 10^{-10} m^2) under a sediment cap. Since the magnitude of the first earthquake is far too small to account for the strain necessary to match the borehole pressure records, *Davis et al.* [2001] conclude that most of the extension occurred aseismically early in the swarm, an inference that is consistent with dike intrusion.

[54] The four hydrothermal temperature time series are all for diffuse vents [*Johnson et al.*, 2001]. At the Beach site, the measurements were obtained in an apparatus that was sealed to the seafloor in a small sediment pond but at the other sites the thermistors were inserted into the base of tubeworm fields. At each site the difference between the measured temperature and ambient ocean temperatures increased by an order of magnitude following the event. The data are quite noisy and it is difficult to identify with certainty the onset of the temperature increase. *Johnson et al.* [2000] estimate that the onset of the thermal responses are delayed by times varying from 4 to 11 days. The Easter Island time series has the highest signal to noise and the data seem compatible with a response that starts growing exponentially soon after the first earthquake. At Beach, the data can be interpreted as showing a small transient coseismic response but the onset of a large increase in temperatures is delayed by 8 days. At the two Clam Bed sites the response is very noisy and complex but the first resolvable increase occurs suddenly after 7–11 days.

[55] Since diffuse fluids are a mixture of a high-temperature end-member with a much larger volume of cold seawater, changes in the temperature of the high-temperature component will have only a small effect on the output temperature. The increased temperature must reflect an increase in the proportion of the high-temperature component. Assuming the flux of the cold seawater component remains constant, *Johnson et al.* [2000] use an approach analogous to equation (31) to infer that temperature data require a 4- to 21-fold increase in the volume flux of the high-temperature component. They infer that the heat output of the Endeavour hydrothermal systems increased by an order of magnitude. However, as I noted in Section 3.3, it may not be appropriate to equate local flux measurements in diffuse vents to a whole vent field. The most recent and sophisticated analysis of the heat flux from the Main Endeavour field [*Veirs*, 2003] shows that diffuse flow accounts for only about one seventh (and certainly no more than one third) of the total heat flux from the field. A large increase in diffuse outflow would lead to a much smaller increase in the total output of the field if the high-temperature flux remained relatively constant.

[56] Because I think the total increase in outflow for the whole vent field is unconstrained, I sought to fit the temperature time series using equation (32) with α a free parameter. Figure 15 shows attempts to fit the shape of the two highest quality time series from the Easter Island and Beach sites with one-dimensional pressure perturbation models for both a transient pressure increase (Figures 4a and 4b) and a permeability increase (Figure 7b). For all of the models, I assumed that the total depth of circulation is 2 km which is consistent with circulation above the axial magma chamber at 2.3–2.6 km depth [*Detrick et al.*, 2002]. For the pressure perturbation model I chose solutions with a pressure increase of 1 MPa at depth while for the permeability increase model I assumed a ninefold increase in upflow permeability at depth. All of the solutions presented have α significantly greater than unity (Figure 15, Table 2). However, by varying the value of α in order to match the data, models with substantially different values

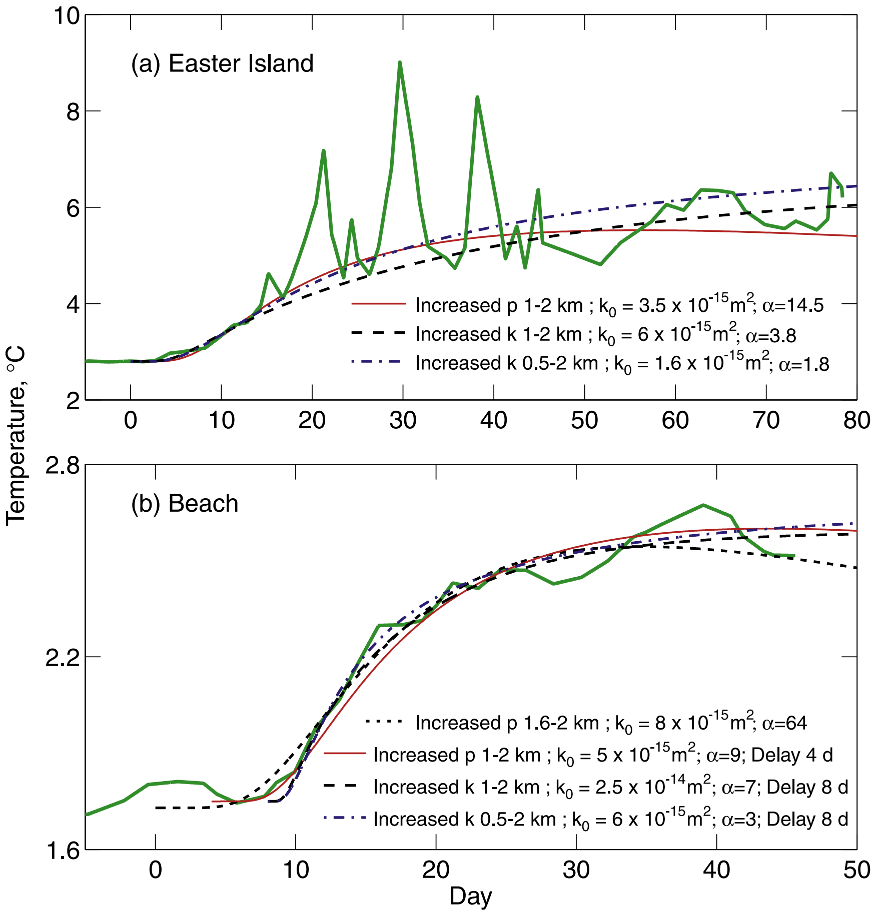

Figure 15. Pressure perturbation models for the diffuse outflow temperature data for the 1999 Endeavour event obtained with equation (32). Times are plotted relative to the first event in the earthquake swarm, and the field data are shown as green bold lines. (a) The temperature data from the Easter Island site are modeled by a pressure increase of 1 MPa at 1–2 km depth (red solid line) and a ninefold increase in permeabilities at 1–2 km depth (black dashed line) and 0.5–2 km depth (blue dot-dashed line) for a system that remains discharge dominated. For each curve the causative event coincides with the time of the first earthquake, and the figure key lists the permeabilities prior to the event and other model parameters. (b) As for Figure 15a except for the Beach site. An additional solution is shown for a pressure perturbation of 1 MPa at 1.6–2 km depth (black dotted), and the times of the causative events are delayed 4–8 days for the other curves as indicated in the key.

for the pressure perturbation or permeability change yield equivalent fits for the same initial permeability.

[57] At Easter Island both types of model can fit the data well for the first 14 days (Table 2) if the causative event coincides with the first earthquake. The required permeability is 10^{-15} to 10^{-14} m^2. After 14 days the models fit the long-term trends but do not reproduce the high-amplitude oscillations seen at this site and also at Clam Bed. To do so would require a complex sequence of shallow pressure perturbations. *Johnson et al.* [2000] interpret these oscillations in terms of subseafloor process and suggest several mechanisms. However, similar oscillations are not observed at the Beach site which was the only site at which the temperatures were measured in an apparatus sealed to the seafloor and so it is perhaps more likely that the oscillations are an artifact of ocean currents.

[58] If the causative event coincides with the first earthquake, the data at the Beach site can only be fit with a transient pressure increase model in which the thickness of the pressurized layer is small compared to its depth. For models with a thicker pressurized layer, it is not possible to fit both the 8 day delay for the onset of the response and the flattening of the temperature curve after 25 days. Such models can fit the data only if the causative event occurred ~4 days into the swarm. The permeability increase model can fit the data only if the permeability change occurs ~8 days

after the first earthquake. The required permeability for both models is 3×10^{-15} to 3×10^{-14} m^2.

[59] There is no unambiguous means to discriminate between the pressure increase and permeability increase models. Both models require permeabilities that are 1–2 orders of magnitude less than the value of $\sim 4 \times 10^{-13}$ m^2 estimated for the Main Endeavour system [*Wilcock and McNabb*, 1995; *Wilcock and Fisher*, 2004], but this may just reflect the relatively low permeability of pathways to the diffuse vent sites. The off-axis borehole data [*Davis et al.*, 2001] require the onset of seismicity to be accompanied by significant strain-induced porosity reductions and it would be surprising if these did not contribute to enhanced outflow at the ridge axis. On the other hand, *Seyfried et al.* [2003] argue that the vapor dominated characteristics of high-temperature fluids from the Main Endeavour field sampled 3 months after the swarm are best explained by reduced and not increased pressures. A decrease in upflow permeability at depth would lead to pressure drops deeper in the system (Figure 7b). The only way to generate a pressure drop at all depths is to decrease the upflow permeability everywhere (Figure 7a) but such a model does not lead to a delayed response and predicts peak outflow immediately following the event.

[60] It is also possible that the observed temperature time series were generated without a significant contribution from pressure perturbations. If the magmatic intrusion caused hot fluids to flow up cracks that were previously cold, it might lead to a substantial increase in diffuse vent temperatures by increasing the flux of high-temperature fluids. Figure 16 shows attempts to fit the temperature data for the Easter Island and Beach sites with the temperature perturbation model. For these models, the term ΔT is only a lower bound on the required temperature perturbation at depth since the temperature perturbations may only affect a fraction of the fluid venting at the diffuse vent. It should be interpreted as $\varepsilon\Delta T$ where ε is the mass fraction of fluid reaching the diffuse vents whose temperature increases by ΔT. At the Easter Island site, the data require crack widths of $\sim$0.6–0.7 mm and after 40 days the data are best fit by a model in which the basal temperature perturbation ramps down in $\sim$100 days. At Beach, the data can be fit by models with crack widths ranging from 0.6 to 0.9 mm depending on the timing of the causative event.

[61] It is clear that the available data for the 1999 Endeavour event do not allow discrimination between the various models discussed in this paper for generating a delayed hydrothermal response. The data can be fit reasonably well with both temperature and pressure perturbation models. Given our understanding of the likely effects of a subseafloor intrusion [e.g., *Germanovich et al.*, 2000], it is conceivable that all the mechanisms discussed in this paper might have contributed to the observed temperature signals (Figure 17). To discriminate between the various mechanisms would require data from a local seismic network in order to identify and characterize the causative earthquake(s) and temperature and flow measurements in high-temperature vents and to understand the relative importance of pressure and temperature perturbations at depth. Time series chemistry measurements would place additional constraints on the fluid flow velocities and the magnitude of subseafloor temperature and pressure changes.

6. Conclusions

[62] In this paper, I have presented two quantitative models for the response of a mid-ocean ridge hydrothermal system to a noneruptive earthquake swarm and I have applied these models to data from two such events. The primary conclusions of this paper are

[63] 1. For the temperature perturbation model the response at the seafloor is markedly different for flow through a planar crack and a circular pipe. For a planar crack, a substantial thermal response is always predicted at the seafloor, but its delay increases as the depth of the perturbation increases and as the crack narrows. For the circular pipe, the thermal response at the seafloor is either observed relatively quickly or barely at all.

[64] 2. For the pressure perturbation model the delay of the seafloor response is dependent on the depth of the pressure anomaly and the permeability. For an anomaly at 1 km depth a permeability of $<\sim 10^{-14}$ m^2 is required to delay the onset of the response a few days.

[65] 3. The 1995 EPR event is well fit by the temperature perturbation model with hydrothermal upflow through a crack with an effective width of 0.6 mm assuming laminar flow. The best fitting model requires that the initial swarm was accompanied by a temperature increase of at least 50°C that decayed over $\sim$16 days. A smaller temperature increase is required at the time of a secondary swarm. One implication of the model is that fluids transit the upflow zone in less than one hour.

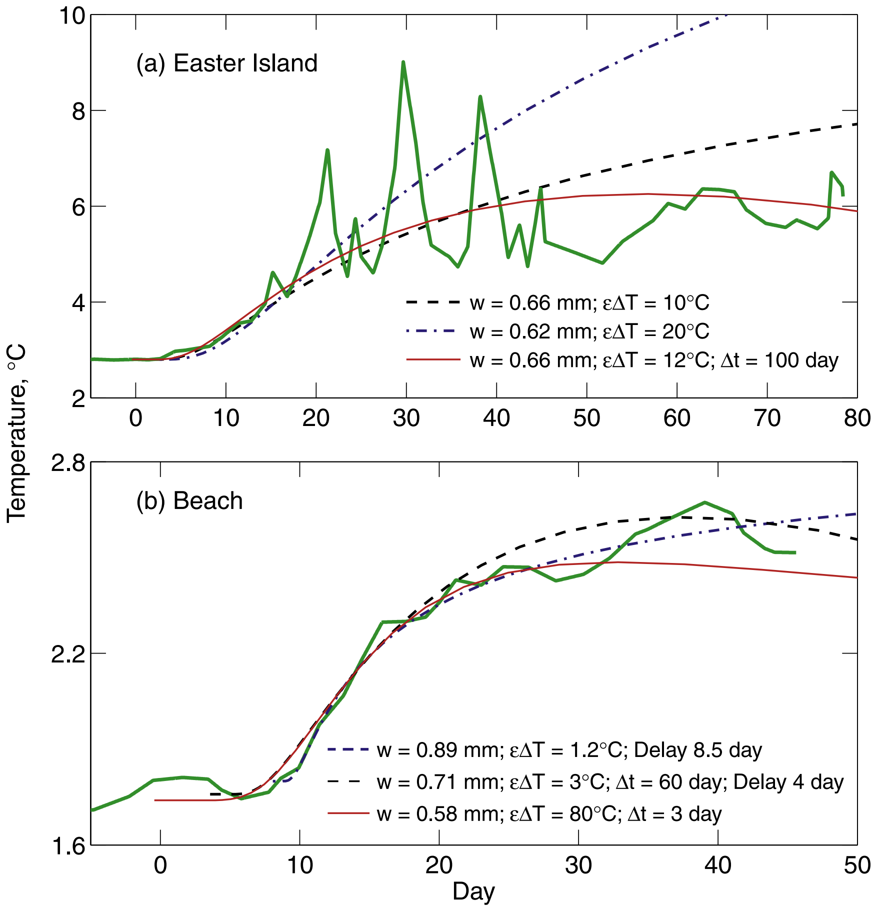

Figure 16. Temperature perturbation models of diffuse outflow temperature data for the 1999 Endeavour event. Times are plotted relative to the first event in the earthquake swarm, and the field data are shown as green bold lines. (a) The temperature data for the Easter Island site are modeled by a temperature perturbation applied to fluids at the base of a 2-km-deep crack. Three curves are shown for different choices of the crack width and effective temperature perturbation ($\varepsilon\Delta T$) as labeled in the key. For the dashed and dot-dashed curves, the temperature perturbation is applied as a step function, while for the solid curve it ramps down linearly over a time Δt = 100 days. (b) As for Figure 16a except for temperature data from the Beach site. The times of the causative events for the dot-dashed and dashed curves are delayed 8.5 and 4 days, respectively. The temperature anomaly for the dashed and solid curves ramp down over 60 and 3 days, respectively.

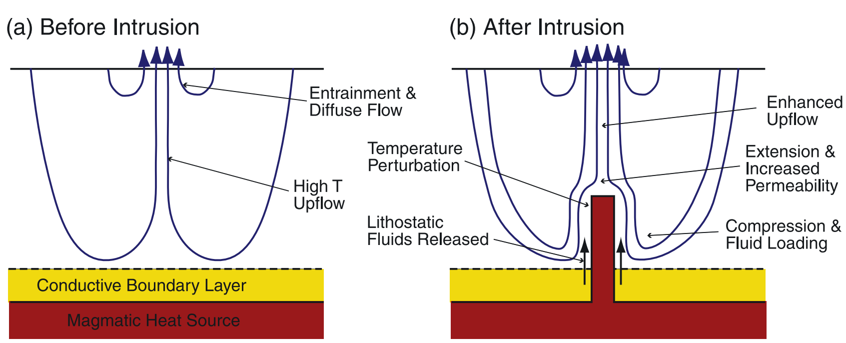

Figure 17. Schematic diagram illustrating the different processes that may have contributed to the hydrothermal response for the 1999 Endeavour event.

[66] 4. The 1999 Endeavour event is less well constrained and the data can be fit equally well by either the temperature perturbation or pressure perturbation models.

[67] 5. Contemporaneous observations from local seismic networks and time series of temperature, fluid fluxes, and chemistry in both high-temperature and diffuse vents will be necessary to constrain fully which mechanisms govern the hydrothermal response to perturbation events and to obtain improved interpretations of the seafloor observations in terms of subseafloor hydrology.

Notation

- a pipe radius, m.
- A cross-sectional area of a hydrothermal upflow or downflow zone, m^2.
- B Skempton's coefficient (equation (24)).
- c_f specific heat capacity of the fluid, J kg^{-1} K^{-1}.
- c_r specific heat capacity of the fluid saturated rock, J kg^{-1} K^{-1}.
- C length scale defined in equations (18) and (20), m.
- d depth below the seafloor, m.
- f_1, f_2 functions defined in equations (11) and (12).
- g acceleration of gravity, m s^{-2}.
- H length scale defined in equations (7) and (9), m.
- k permeability, m^2.
- L fracture spacing, m.
- K drained bulk modulus of the fluid saturated porous medium, Pa.
- K_f bulk modulus of the fluid, Pa.
- K_s unjacketed bulk modulus (bulk modulus of the solid grains), Pa.
- K_ϕ unjacketed bulk modulus of the pores, Pa.
- K_0 modified Bessel function of the second kind.
- p nonhydrostatic pressure, Pa.
- q Darcy velocity or volumetric outflow flux, m s^{-1}.
- q_0 Volumetric outflow flux prior to an event, m s^{-1}.
- r radial coordinate for the pipe model, m.
- R flow resistance of a hydrothermal upflow or downflow zone, kg m^{-4} s^{-1}.
- S specific storage, Pa^{-1}.
- t time, s.
- t_p period of a temperature perturbation, s.
- T temperature, °C.
- T_b temperature at the base of the conduit, °C.
- T_c temperature of cold seawater, °C.
- T_u upflow temperature prior to conductive cooling, °C.
- T_v venting temperature, °C.
- $\bar{u}$ mean flow velocity up the crack or pipe, m s^{-1}.
- w crack width, m.
- x horizontal coordinate for the crack model, m.
- z vertical coordinate, m.
- Δp pressure perturbation, Pa.
- Δt time for temperature perturbation to ramp down, s.
- ΔT temperature perturbation, °C.
- α term in equation (32).
- ϵ mass fraction of fluid venting at a diffuse vent whose temperature is perturbed.
- ζ, η functions defined in equations (16) and (17).
- θ fault dip.
- κ thermal diffusivity of the fluid saturated rock, m s^{-2}.
- λ thermal conductivity of the fluid saturated rock, W m^{-1} K^{-1}.
- μ dynamic viscosity of the fluid, Pa s.
- ν Poisson's ratio.
- ρ_f density of hydrothermal fluid, kg m^{-3}.
- ρ_r density of the fluid saturated rock, kg m^{-3}.
- σ normal stress, Pa.
- τ shear stress, Pa.
- ϕ porosity.
- ω angular frequency of the temperature perturbation, s^{-1}.

Acknowledgments

[68] This work was motivated by seminar given by Matt Pruis. I thank Del Bohnenstiehl, Dan Fornari, Paul Johnson, and Rob Sohn for providing data; Andrew Barclay, Fabrice Fontaine, and Tim Crone for useful discussions; and Leonid Germanovich, an anonymous reviewer, and Associate Editor Mike Gurnis for insightful reviews.

References

Aggarwal, Y. P., L. R. Sykes, J. Armbruster, and M. L. Sbar (1973), Premonitory changes in seismic velocities and prediction of earthquakes, *Nature*, *241*, 101–104.

Anderko, A., and K. S. Pitzer (1993), Equation-of-state representation of phase equilibria and volumetric properties of the system NaCl-H_20 above 573 K, *Geochim. Cosmochim. Acta*, *57*, 1657–1680.

Arfken, G. (1985), *Mathematical Methods for Physicists*, 985 pp., Academic, San Diego, Calif.

Baker, E. T., G. J. Massoth, and R. A. Feely (1987), Cataclysmic hydrothermal venting on the Juan de Fuca Ridge, *Nature*, *329*, 149–151.

Baker, E. T., J. W. Lavelle, R. A. Feely, G. J. Massoth, S. L. Walker, and J. E. Lupton (1989), Episodic venting of hydrothermal fluids from the Juan de Fuca Ridge, *J. Geophys. Res.*, *94*, 9237–9250.

Baker, E. T., G. J. Massoth, R. A. Feely, R. W. Embley, R. E. Thomson, and B. J. Burd (1995), Hydrothermal event plumes from the CoAxial seafloor eruption site, Juan de Fuca Ridge, *Geophys. Res. Lett.*, *22*, 147–150.

Baker, E. T., C. G. Fox, and J. P. Cowen (1999), In situ observations of the onset of hydrothermal discharge during the 1998 submarine eruption of Axial Volcano, Juan de Fuca Ridge, *Geophys. Res. Lett.*, *26*, 3445–3448.

Becker, K. (1985), Large-scale electrical resistivity and bulk porosity of the oceanic crust, Deep Sea Drilling Project Hole 504B, Costa Rica Rift, *Initial Rep. Deep Sea Drill. Proj.*, *83*, 419–427.

Bohnenstiehl, D. R., M. Tolstoy, R. P. Dziak, C. G. Fox, and D. K. Smith (2001), The June 1999 Endeavour earthquake sequence: Evidence for a non-tectonic origin, *Eos Trans. AGU*, *82*(47), Fall Meet Suppl., Abstract S22C-06.

Bohnenstiehl, D. R., M. Tolstoy, R. P. Dziak, C. G. Fox, and D. K. Smith (2002), Aftershock sequences in the mid-ocean ridge environment: An analysis using hydroacoustic data, *Tectonophysics*, *354*, 49–70.

Bohnenstiehl, D. R., R. P. Dziak, M. Tolstoy, C. G. Fox, and M. Fowler (2004), Temporal and spatial history of the 1999–2000 Endeavour Segment seismic series, Juan de Fuca Ridge, *Geochem. Geophys. Geosyst.*, *5*, Q09003, doi:10.1029/2004GC000735.

Brune, J. N. (1970), Tectonic stress and the spectra of seismic shear waves from earthquakes, *J. Geophys. Res.*, *75*, 4997–5009.

Carlslaw, H. S., and J. C. Jaeger (1938), Some problems in the mathematical theory of the conduction of heat, *Philos. Mag. Ser. 7*, *26*, 473–495.

Carlslaw, H. S., and J. C. Jaeger (1959), *Conduction of Heat in Solids*, 510 pp., Clarendon, Oxford, England.

Carlson, R. L., and C. N. Herrick (1990), Densities and porosities in the oceanic crust and their variations with depth and age, *J. Geophys. Res.*, *95*, 9153–9170.

Carlson, D. R., S. E. Widnall, and M. F. Peeters (1982), A flow-visualization study of transition in plane Poiseuille flow, *J. Fluid Mech.*, *121*, 487–505.

Clauser, C., and E. Huenges (1995), Thermal conductivity of rocks and minerals, in *Rock Physics and Phase Relations: A Handbook of Physical Constants*, *AGU Ref. Shelf*, vol. 3, edited by T. J. Ahrens, pp. 105–126, AGU, Washington, D. C.

Cowen, J. P., E. T. Baker, and R. W. Embley (2004), Detection of and response to mid-ocean ridge magmatic events: Implications for the subsurface biosphere, in *The Subseafloor Biosphere at Mid-Ocean Ridges*, *Geophys. Monogr. Ser.*, vol. 144, edited by W. S. D. Wilcock et al., pp. 227–243, AGU, Washington, D. C.

Crone, T. J., and W. S. D. Wilcock (2002), Modeling the effects of tidal loading on hydrothermal discharge at mid-ocean ridges, *Eos Trans. AGU*, *83*(47), Fall Meet. Suppl., H21B-0808.

Curewitz, D., and J. A. Karson (1998), Geological consequences of dike intrusions at mid-ocean ridge spreading centers, in *Faulting and Magmatism at Mid-Ocean Ridges*, *Geophys. Monogr. Ser.*, vol. 106, edited by W. R. Buck et al., pp. 117–136, AGU, Washington, D. C.

Davis, E. E., W. Wang, R. E. Thomson, K. Becker, and J. F. Cassidy (2001), An episode of seafloor spreading and associated plate deformation inferred from crustal fluid pressure transients, *J. Geophys. Res.*, *106*, 21,953–21,963.

Detrick, R. S., P. Buhl, E. Vera, J. Mutter, J. Orcutt, J. Madsen, and T. Brocher (1987), Multi-channel seismic imaging of a crustal magma chamber along the East Pacific Rise, *Nature*, *326*, 35–41.

Detrick, R. S., S. Carbotte, E. V. Ark, J. P. Canales, G. Kent, A. Harding, J. Diebold, and M. Nedimovic (2002), New multichannel seismic constraints on the crustal structure of the Endeavour segment, Juan de Fuca Ridge: Evidence for a crustal magma chamber, *Eos Trans. AGU*, *83*(47), Fall Meet. Suppl., Abstract T12B-1316.

Dziak, R. P., and H. P. Johnson (2002), Stirring the oceanic incubator, *Science*, *296*, 1406–1407.

Embley, R., and E. Baker (1999), Interdisciplinary group explores seafloor eruption with remotely operated vehicle, *Eos Trans. AGU*, *80*, 213, 219–222.

Fornari, D. J., T. Shank, K. L. Von Damm, T. K. P. Gregg, M. Lilley, G. Levai, A. Bray, R. M. Haymon, M. R. Perfit, and R. Lutz (1998), Time-series temperature measurements at high temperature hydrothermal vents, East Pacific Rise 9°49′–51′N: Evidence for monitoring a crustal cracking event, *Earth Planet Sci. Lett.*, *160*, 419–431.

Fox, C. G. (1999), In situ ground deformation measurements from the summit of Axial Volcano during the 1998 volcanic episode, *Geophys. Res. Lett.*, *26*, 3437–3440.

Fox, C. G., R. P. Dziak, H. Marumoto, and A. E. Schreiner (1994), Potential for monitoring low-level seismicity on the Juan de Fuca Ridge using military hydrophone arrays, *Mar. Technol. Soc. J.*, *27*(4), 22–30.

Germanovich, L. N., R. P. Lowell, and D. K. Astakhov (2000), Stress-dependent permeability and the formation of event plumes, *J. Geophys. Res.*, *105*, 8341–8354.

Goldfarb, M. S., and J. R. Delaney (1988), Response of two-phase fluids to fracture configurations within submarine hydrothermal systems*J. Geophys. Res.*, *93*, 4585–4594.

Johnson, H. P., M. Hutnak, R. P. Dziak, C. G. Fox, I. Urcuyo, J. P. Cowen, J. Nabalek, and C. Fisher (2000), Earthquake-induced changes in a hydrothermal system on the Juan de Fuca Ridge mid-ocean ridge, *Nature*, *407*, 174–177.

Johnson, H. P., R. P. Dziak, C. R. Fisher, C. G. Fox, and M. J. Pruis (2001), Earthquakes' impact on hydrothermal systems may be far-reaching, *Eos Trans. AGU*, *82*, 233–236.

Lavelle, J. W. (1995), The initial rise of a hydrothermal plume from a line segment source: Results from a three-dimensional numerical model, *Geophys. Res. Lett.*, *22*, 159–162.

Lilley, M. D., D. A. Butterfield, J. E. Lupton, and E. J. Olson (2003), Magmatic events can produce rapid changes in hydrothermal vent chemistry, *Nature*, *422*, 878–881.

Lister, C. R. B. (1974), On the penetration of water into hot rock, *Geophys. J. R. Astron. Soc.*, *39*, 465–509.

Lister, C. R. B. (1983), The basic physics of water penetration into hot rocks, in *Hydrothermal Processes at Seafloor Spreading Centers*, edited by P. A. Rona et al., pp. 141–168, Plenum, New York.

Lowell, R. P., and L. N. Germanovich (1994), On the temporal evolution of high-temperature hydrothermal systems at ocean ridge crests, *J. Geophys. Res.*, *99*, 565–575.

Lowell, R. P., and L. N. Germanovich (1995), Dike injection and the formation of megaplumes at ocean ridges, *Science*, *267*, 1804–1807.

Lowell, R. P., P. A. Rona, and R. P. Von Herzen (1995), Seafloor hydrothermal systems *J. Geophys. Res.*, *100*, 327–352.

Lupton, J., E. Baker, R. Embley, R. Greene, and L. Evans (1999a), Anomalous helium and heat signatures associated with the 1998 Axial Volcano event, Juan de Fuca Ridge, *Geophys. Res. Lett.*, *26*, 3449–3452.

Lupton, J. E., E. T. Baker, and G. J. Massoth (1999b), Helium, heat, and the generation of hydrothermal event plumes at mid-ocean ridges, *Earth Planet Sci. Lett.*, *171*, 343–350.

Massoth, G. J., E. T. Baker, R. A. Feely, D. A. Butterfield, R. E. Embley, J. E. Lupton, R. E. Thomson, and G. A. Cannon (1995), Observations of manganese and iron at the CoAxial seafloor eruption site, Juan de Fuca Ridge, *Geophys. Res. Lett.*, *22*, 151–154.

Meyer, C. A., R. B. McClintock, G. J. Silvestri, and R. C. Spencer Jr. (1993), *ASME Steam Tables: Thermodynamic and Transport Properties of Steam*, 436 pp., Am. Soc. of Mech. Eng., New York.

Muir-Wood, R., and G. C. P. King (1993), Hydrological signatures of earthquake strain, *J. Geophys. Res.*, *98*, 22,035–22,068.

Nehlig, P. (1994), Fracture and permeability analysis in magma-hydrothermal transition zones in the Samail ophiolite (Oman), *J. Geophys. Res.*, *99*, 589–601.

Nur, A. (1972), Dilatancy, pore fluids, and premonitory variations of t_S/t_P travel times, *Bull. Seismol. Soc. Am.*, *62*, 1217–1222.

Orszag, S. A. (1971), Accurate solutions of the Orr-Sommerfeld stability equation, *J. Fluid Mech.*, *50*, 689–703.

Palmer, M. R., and G. G. J. Ernst (1998), Generation of hydrothermal megaplumes by cooling of pillow basalts at mid-ocean ridges, *Nature*, *393*, 643–647.

Palmer, M. R., G. G. J. Ernst, J. E. Lupton, E. T. Baker, and G. J. Massoth (2000), Helium, heat and the generation of hydrothermal event plumes at mid-ocean ridges: Discussion and reply, *Earth Planet. Sci. Lett.*, *180*, 215–222.

Petrunin, G. I., V. G. Popov, and V. M. Ladygin (2001), Thermal properties of basalts from the Bouvet triple junction and their implications for petrophysical characteristics, *Izv. Phys. Solid Earth*, *37*, 441–451.

Roeloffs, E. (1996), Poroelastic techniques in the study of earthquake-related hydrologic phenomena, in *Advances in Geophysics*, edited by R. Dmowska and B. Saltzman, pp. 135–195, Academic, San Diego, Calif.

Rubin, A. M., and D. D. Pollard (1987), Origins of blade-like dikes in volcanic rift zones, in *Volcanism in Hawaii*, edited by R. W. Decker, T. L. Wright, and P. H. Stauffer, *U.S. Geol. Surv. Prof. Pap.*, *1350*, 1149–1470.

Seyfried, W. E., Jr., and W. C. Shanks III (2004), Alteration and mass transport in high-temperature hydrothermal systems at mid-ocean ridges: Controls on the chemical and isotopic evolution of axial vent fields, in *The Hydrogeology of the Oceanic Lithosphere*, edited by E. E. Davis and H. Elderfield, Cambridge Univ. Press, New York, in press.

Seyfried, W. E., Jr., J. S. Seewald, M. E. Berndt, K. Ding, and D. I. Foustoukos (2003), Chemistry of hydrothermal vent fluids from the Main Endeavour Field, northern Juan de Fuca Ridge: Geochemical controls in the aftermath of June 1999 seismic events, *J. Geophys. Res.*, *108*(B9), 2429, doi:10.1029/2002JB001957.

Sibson, R. H., J. M. Moore, and A. H. Rankin (1975), Seismic pumping—A hydrothermal fluid transport mechanism, *J. Geol. Soc. London*, *131*, 653–659.

Sohn, R. A., D. J. Fornari, K. L. Von Damm, J. A. Hildebrand, and S. C. Webb (1998), Seismic and hydrothermal evidence for a cracking event on the East Pacific rise crest at 9°50′N, *Nature*, *396*, 159–161.

Sohn, R. A., J. A. Hildebrand, and S. C. Webb (1999), A microearthquake survey of the high-temperature vent fields on the volcanically active East Pacific Rise, *J. Geophys. Res.*, *104*, 25,367–25,377.

Turcotte, D. L., and G. Schubert (1982), *Geodynamics: Applications of Continuum Mechanics to Geological Problems*, 450 pp., John Wiley, New York.

Veirs, S. R. (2003), Heat flux and hydrography at a submarine volcano: Observations and models of the Main Endeavour vent field in the northeast Pacific, Ph.D. thesis, Univ. of Wash., Seattle, Wash.

Wang, H. F. (2000), *Theory of Linear Poroelasticity With Applications to Geomechanics and Hydrogeology*, 276 pp., Princeton Univ. Press, Princeton, N. J.

Wilcock, W. S. D. (1998), Cellular convection models of mid-ocean ridge hydrothermal circulation and the temperatures of black smoker fluids, *J. Geophys. Res.*, *103*, 2585–2596.

Wilcock, W. S. D., and A. T. Fisher (2004), Geophysical constraints on the sub-seafloor environment near mid-ocean ridges, in *The Subseafloor Biosphere at Mid-Ocean Ridges*, *Geophys. Monogr. Ser.*, vol. 144, edited by W. S. D. Wilcock et al., pp. 51–74, AGU, Washington, D. C.

Wilcock, W. S. D., and A. McNabb (1995), Estimates of crustal permeability on the Endeavour segment of the Juan de Fuca mid-ocean ridge, *Earth Planet. Sci. Lett.*, *138*, 83–91.